

# Chapter 15

## Current Density Reconstruction

*From Magnetic Field Maps to Source Currents*

This chapter applies the general reconstruction framework of Chapter 14 to the **specific inverse problem of current density reconstruction (CDR)**, completing the QFI operator stack for its defining application: transforming magnetic field maps  $\vec{B}(\vec{r})$  into source current distributions  $\vec{J}(\vec{r})$  with quantified, traceable uncertainty.

### **Operator Focus:**

- **Physics operator  $G$ :** Biot–Savart kernel with Fourier-space transfer function  $\tilde{G}(k) = (\mu_0/2) e^{-|k|z_0}/|k|$  and exponential ill-conditioning  $\kappa \sim e^{k_{\max} z_0}$  (Sections 15.2–15.3)
- **Measurement operator  $H$ :** Composite transfer function  $H = H_{\text{ODMR}} \circ H_{\text{depth}} \circ H_{\text{pixel}} \circ H_{\text{PSF}}$  for traceable uncertainty propagation (Section 15.3)
- **Reconstruction operator  $R$ :** 2D Fourier inversion, Wiener filtering, 3D iterative ADMM, and CAD-informed priors (Sections 15.4–15.7)
- **Validation operator  $V$ :** Auditable falsification protocol with  $\chi^2$ , whiteness, and localised cluster test statistics; production parameter lock (Sections 15.9–15.10)

### **Key Achievements:**

- Complete forward model  $\mathbf{b}_{\text{meas}} = H \cdot G[\vec{J}] + \epsilon$  unifying Biot–Savart physics with the optical/sensor measurement chain
- 2D Fourier-space inversion with boundary treatment achieving  $\Gamma_{\text{inv}} \approx 0.85$  in  $< 0.1$  s
- Multi-physics depth disambiguation: combining  $\vec{B}$  with  $\Delta T$  improves  $\Gamma_{\text{inv}}$  from 0.62 to 0.91
- Vector reconstruction from 4-axis NV measurements boosting  $\Gamma_{\text{inv}}$  by  $\sim 10\%$  with out-of-plane current detection
- CAD-informed priors achieving  $\Gamma_{\text{inv}} > 0.90$  under specified conditions ( $z_0 \leq 10 \mu\text{m}$ , SNR  $\geq 50$ , registration error  $< 0.5 \mu\text{m}$ )
- Standoff non-uniformity analysis quantifying the dominant production systematic ( $\Delta z/z_0 > 15\%$  degrades  $P_{95}$  below 90%)
- Three worked examples spanning 2D graphene imaging, 3D IC failure analysis, and CAD-mismatch defect discovery

Current density reconstruction is the defining application that promotes Quantum Field Metrology (QFM) to true Quantum Field Imaging (QFI). A system that delivers only  $\vec{B}(\vec{r})$  maps—however parallel, however sensitive—remains QFM. It is the reconstruction operator  $R$ , together with per-pixel uncertainty quantification  $\sigma_J(\vec{r})$  and auditable falsification testing, that completes the QFI pipeline and enables the engineering question: “*What is there, where exactly, and how much current flows?*”

### **QFI Pipeline Position:**

$$S(\vec{r}) \xrightarrow{G} F(\vec{r}) \xrightarrow{M} D \xrightarrow{\boxed{R}} \hat{S}(\vec{r}) \pm \sigma_S$$

where  $S = \vec{J}$  (current density),  $G$  is the Biot–Savart operator,  $F = \vec{B}$  (magnetic field),  $M = H$  is the measurement operator (PSF  $\circ$  pixel  $\circ$  depth  $\circ$  ODMR),  $D = \mathbf{b}_{\text{meas}}$  is the measured data, and  $R$  (this chapter) reconstructs  $\hat{S} = \hat{\vec{J}}$  with traceable uncertainty  $\sigma_J$ .

**Central Metric:** Reconstruction fidelity  $\Gamma_{\text{inv}} = \text{CRB}/\text{MSE}_{\text{achieved}}$ , with production target  $\Gamma_{\text{inv}} > 0.85$  and  $P_{95}$  coverage  $> 90\%$  validated on golden samples.

| Abbrev.              | Definition                                  | Abbrev.               | Definition                    |
|----------------------|---|-----------------------|-------------------------------|
| QFI                  | Quantum Field Imaging                       | QFM                   | Quantum Field Metrology       |
| CDR                  | Current Density Reconstruction              | BS                    | Biot–Savart (law/kernel)      |
| FIM                  | Fisher Information Matrix                   | CRB                   | Cramér–Rao Bound              |
| UQ                   | Uncertainty Quantification                  | TV                    | Total Variation               |
| CAD                  | Computer-Aided Design                       | IC                    | Integrated Circuit            |
| TSV                  | Through-Silicon Via                         | NV                    | Nitrogen-Vacancy (center)     |
| FFT                  | Fast Fourier Transform                      | SNR                   | Signal-to-Noise Ratio         |
| ADMM                 | Alternating Direction Method of Multipliers | PSF                   | Point Spread Function         |
| DOF                  | Degrees of Freedom                          | GPU                   | Graphics Processing Unit      |
| PINN                 | Physics-Informed Neural Network             | OTF                   | Optical Transfer Function     |
| ODMR                 | Optically Detected Magnetic Resonance       | GCV                   | Generalized Cross-Validation  |
| QDM                  | Quantum Diamond Microscope                  | PRNU                  | Photo-Response Non-Uniformity |
| PSD                  | Power Spectral Density                      | $\Gamma_{\text{inv}}$ | Reconstruction Fidelity       |
| $\Gamma_{\text{mm}}$ | Model-Mismatch Penalty                      | $Q_{\text{IFOM}}$     | QFI Imaging Figure of Merit   |

Table 15.1: Abbreviated terms used in Chapter 15.

## Abstract

This chapter applies the general reconstruction framework developed in Chapter 14 to the specific inverse problem of current density reconstruction (CDR) from magnetic field measurements. Current density imaging represents the quintessential QFI application, transforming measured magnetic field maps  $\vec{B}(\vec{r})$  into source current distributions  $\vec{J}(\vec{r})$  with quantified uncertainty. We develop the complete forward model including both the Biot–Savart physics operator  $G$  and the measurement operator  $H$  (optical PSF, pixel aperture, NV depth distribution, and ODMR fit pipeline), enabling traceable uncertainty propagation. Specialized algorithms exploit the kernel structure, covering both 2D planar inversions (fast Fourier methods with boundary treatment) and 3D depth-resolved reconstructions (iterative algorithms with multi-physics regularization). Standoff non-uniformity analysis quantifies sensitivity to the dominant production systematic. Vector reconstruction from four-axis NV measurements enables complete  $\vec{J} = (J_x, J_y, J_z)$  recovery. CAD-informed priors achieve reconstruction fidelity  $\Gamma_{\text{inv}} > 0.90$  for IC applications under specified conditions (standoff  $z_0 \leq 10 \mu\text{m}$ , SNR  $\geq 50$ , CAD registration error  $< 0.5 \mu\text{m}$ ). An auditable falsification protocol with explicit test statistics upgrades CDR from reconstruction to metrology. Three worked examples bracket the application space from 2D graphene imaging through 3D IC failure analysis to CAD-mismatch defect discovery workflows. Validation protocols using golden samples establish traceable  $\Gamma_{\text{inv}}$  benchmarks for production QFI systems.

## 15.1 Introduction and Motivation

### 15.1.1 Why Current Density Reconstruction Matters

Current density reconstruction represents the defining application that transforms a Quantum Field Metrology (QFM) system into true Quantum Field Imaging (QFI). While magnetic field mapping (QFM) provides valuable information—identifying that “something is there”—current density reconstruction (QFI) answers the engineering question: “*What* is there, *where* exactly, and *how much* current flows?”

**Definition 15.1.1** (Current Density Reconstruction). Current Density Reconstruction (CDR) is the inverse problem of determining the source current density distribution  $\vec{J}(\vec{r})$  from measured magnetic field data  $\vec{B}_{\text{meas}}(\vec{r})$ , with quantified reconstruction uncertainty  $\sigma_J(\vec{r})$ :

$$\text{CDR} : \quad \vec{B}_{\text{meas}}(\vec{r}) \xrightarrow{\mathbf{R}} \hat{\mathbf{J}}(\vec{r}) \pm \sigma_J(\vec{r}) \quad (15.1)$$

where  $\mathbf{R}$  is the reconstruction operator completing the QFI pipeline.

### 15.1.2 Historical Context and Key Developments

The mathematical foundation for current reconstruction from magnetic fields dates to Ampère’s work in the 1820s, but practical implementation required modern sensing capabilities:

- **1820s:** Ampère and Biot–Savart establish the forward relationship  $\vec{B}(\vec{r}) = G[\vec{J}(\vec{r})]$ .
- **1960s–1980s:** SQUID magnetometers enable first magnetic microscopy for current imaging. Roth, Sepulveda, and Wikswo [[15.4]] demonstrate 2D current reconstruction from SQUID data, establishing the Fourier-space inversion framework.
- **2008:** First NV-based magnetic imaging demonstrations by Maze et al. [[15.7]] and Balasubramanian et al. [[15.8]], opening the path to wide-field quantum magnetic microscopy.
- **2017:** Wide-field current imaging in graphene by Tetienne et al. [[15.1]] demonstrates 2D CDR with NV ensembles, achieving sub-micrometre resolution.
- **2020:** Vector reconstruction protocols established by Broadway et al. [[15.2]] using 4-axis NV measurements, improving  $\Gamma_{\text{inv}}$  by  $\sim 10\%$ .
- **2021:** NV-based current imaging applied to integrated circuits by Nowodzinski et al. [[15.13]], demonstrating IC failure analysis capability.
- **2022–2024:** CAD-informed reconstruction and optimised widefield CDR pipelines emerge [[15.3], [15.14]], achieving  $\Gamma_{\text{inv}} > 0.9$  for IC applications.

### 15.1.3 Pain Points in Current Density Reconstruction

CDR faces fundamental challenges arising from the physics of magnetic field propagation:

1. **Ill-Posedness:** The Biot–Savart kernel acts as a low-pass filter; high spatial frequencies are exponentially attenuated with standoff distance  $z_0$ , leading to condition numbers  $\kappa \sim e^{k_{\max} z_0}$ .
2. **Depth Ambiguity:** 2D magnetic measurements at a single plane cannot uniquely determine 3D current distributions—infinitely many  $\vec{J}(x, y, z)$  configurations produce identical  $B_z(x, y)$ .

3. **Vector Incompleteness:** Single-axis NV projections measure only  $\vec{B} \cdot \hat{n}$ ; full vector reconstruction requires combining measurements from all four NV crystallographic orientations.
4. **Noise Amplification:** Naive inversion amplifies measurement noise by factor  $\sim \kappa$ , making regularization essential.
5. **Model Mismatch:** Real IC geometries deviate from idealised models, introducing systematic reconstruction errors quantified by  $\Gamma_{\text{mm}}$ .
6. **Measurement Operator Blur:** The measured field map is not the true field  $F(\vec{r})$  but a blurred, sampled, depth-averaged version  $H[F(\vec{r})]$ ; ignoring  $H$  produces biased uncertainty estimates.

#### 15.1.4 Figures of Merit for CDR

Table 15.2 defines the key performance metrics for current density reconstruction.

Table 15.2: Figures of merit for current density reconstruction.

| Metric                  | Symbol                  | Units                               | Description  |
|-------------------------|-------------------------|-------------------------------------|--|
| Reconstruction fidelity | $\Gamma_{\text{inv}}$   | Dimensionless                       | $1 - \ \hat{\mathbf{J}} - J_{\text{true}}\  / \ J_{\text{true}}\ $ |
| Current sensitivity     | $\eta_J$                | A/m <sup>2</sup> /Hz <sup>1/2</sup> | Minimum detectable current density per unit bandwidth              |
| Spatial resolution      | $\delta_J$              | $\mu\text{m}$                       | FWHM of current-density PSF  |
| Depth resolution        | $\delta_z$              | $\mu\text{m}$                       | $z$ -axis discrimination capability                                |
| Localisation accuracy   | $\epsilon_{\text{loc}}$ | $\mu\text{m}$                       | RMS position error for point sources                               |
| Uncertainty coverage    | $P_{95}$                | %                                   | Fraction of true values within 95% confidence interval             |
| Computation time        | $t_{\text{recon}}$      | s                                   | Wall-clock time for single reconstruction                          |

*Remark 15.1.1* (Measurement Protocol for  $\eta_J$ ). The current sensitivity  $\eta_J$  is defined as the current density that produces a reconstructed signal equal to one standard deviation of the reconstruction noise, per unit measurement bandwidth:

$$\eta_J = \frac{\sigma_J}{\sqrt{\Delta f}} \quad (15.2)$$

where  $\sigma_J$  is the RMS reconstruction noise ( $\text{A}/\text{m}^2$ ) in a field region with no current, and  $\Delta f = 1/(2t_{\text{int}})$  is the measurement bandwidth set by the integration time  $t_{\text{int}}$ . Reporting  $\eta_J$  requires specifying  $t_{\text{int}}$ , pixel size, standoff  $z_0$ , and regularization parameter  $\lambda$ .

#### Design Rule 1: QFI Completeness Criterion

A current density reconstruction system qualifies as QFI only if it provides **all four outputs**:

1. Source estimate  $\hat{\mathbf{J}}(\vec{r})$
2. Uncertainty bounds  $\sigma_J(\vec{r})$  with specified confidence level

3. Reconstruction residual  $\|\vec{B}_{\text{meas}} - H \cdot G[\hat{\mathbf{J}}]\|$
4. Falsification test result (pass/fail with  $p$ -value; see Section 15.9.4)

Systems providing only  $\hat{\mathbf{J}}(\vec{r})$  without uncertainty quantification remain QFM, not QFI.

### 15.1.5 Engineering Sanity Checklist

Table 15.3 provides order-of-magnitude reference values for rapid sanity checking of CDR inputs and outputs.

Table 15.3: Engineering sanity checklist for CDR.

| Quantity   | Typical Range  | Quick Check   |
|--|--|---|
| $B_z$ from 1 mA wire at $z_0 = 5 \mu\text{m}$                    | $\sim 80 \text{ nT}$                                 | $\approx \mu_0 I / (2\pi z_0)$  |
| Widefield NV noise floor   | $1\text{--}100 \text{ nT}/\sqrt{\text{Hz}}$          | Depends on NV density, contrast, $t_{\text{int}}$   |
| Practical $k$ -space cutoff<br>Wiener parameter $\lambda$        | $k_c \approx 1/(2\pi z_0)$<br>$10^{-3}$ to $10^{-1}$ | $\approx 0.032 \mu\text{m}^{-1}$ for $z_0 = 5 \mu\text{m}$<br>L-curve or GCV inflection point |
| Pixel size (widefield NV)  | $0.1\text{--}1 \mu\text{m}$                          | Set by magnification $\times$ camera pitch  |
| $\Gamma_{\text{inv}}$ pass threshold                             | $> 0.85$   | With $P_{95} > 90\%$ on golden sample   |
| $J$ from 1 mA in 1 $\mu\text{m}$ wire<br>(1 $\mu\text{m}$ thick) | $10^9 \text{ A/m}^2$                                 | $= I/(w \times t)$  |

## 15.2 The Biot–Savart Forward Model

### 15.2.1 Continuous Formulation

The magnetic field  $\vec{B}$  generated by a current density distribution  $\vec{J}$  is given by the Biot–Savart law:

#### Key Equation: Biot–Savart Law

$$\vec{B}(\vec{r}) = \frac{\mu_0}{4\pi} \int_V \frac{\vec{J}(\vec{r}') \times (\vec{r} - \vec{r}')}{| \vec{r} - \vec{r}' |^3} d^3 r' \quad (15.3)$$

where  $\mu_0 = 4\pi \times 10^{-7} \text{ T}\cdot\text{m/A}$  is the permeability of free space.

For a current sheet at  $z' = 0$  measured at height  $z = z_0$ , the  $z$ -component of magnetic field is:

$$B_z(x, y, z_0) = \frac{\mu_0}{4\pi} \iint \frac{J_y(x', y')(x - x') - J_x(x', y')(y - y')}{[(x - x')^2 + (y - y')^2 + z_0^2]^{3/2}} dx' dy' \quad (15.4)$$

This is a convolution integral, enabling efficient computation via FFT.

### 15.2.2 Fourier-Space Representation

In Fourier space, Eq. (15.4) simplifies to algebraic products:

**Key Equation: Biot–Savart in Fourier Space**

$$\tilde{B}_z(k_x, k_y) = \frac{\mu_0}{2} (ik_x \tilde{J}_y - ik_y \tilde{J}_x) \frac{e^{-|\vec{k}|z_0}}{|\vec{k}|} \quad (15.5)$$

where  $|\vec{k}| = \sqrt{k_x^2 + k_y^2}$  and tildes denote 2D Fourier transforms.

The exponential decay  $e^{-|\vec{k}|z_0}$  is the fundamental source of ill-posedness: spatial frequencies with  $|\vec{k}|z_0 \gg 1$  are exponentially suppressed, requiring regularisation for stable inversion.

We define the Biot–Savart transfer function as:

$$\tilde{G}(k) = \frac{\mu_0}{2} \frac{e^{-|k|z_0}}{|k|} \quad (15.6)$$

so that  $\tilde{B}_z = \tilde{G}(k) \cdot (ik_x \tilde{J}_y - ik_y \tilde{J}_x)$ .

**15.2.3 Discretisation for Computation**

For numerical implementation on an  $N_x \times N_y$  grid with pixel size  $\Delta$ , the discrete forward model is:

$$\mathbf{b} = \mathbf{G}\mathbf{j} + \boldsymbol{\epsilon} \quad (15.7)$$

where  $\mathbf{b} \in \mathbb{R}^N$  is the vectorised field map,  $\mathbf{G} \in \mathbb{R}^{N \times 2N}$  is the discrete Biot–Savart operator (factor 2 from  $J_x, J_y$  components), and  $\boldsymbol{\epsilon} \sim \mathcal{N}(0, \sigma_B^2 \mathbf{I})$  is measurement noise.

The condition number of  $\mathbf{G}$  grows as:

$$\kappa(\mathbf{G}) \sim \frac{e^{k_{\max} z_0}}{e^{k_{\min} z_0}} \approx e^{k_{\max} z_0} \quad (15.8)$$

where  $k_{\max} = \pi/\Delta$  is the Nyquist frequency.

**15.3 Measurement Operator and Traceable Forward Model**

In real widefield NV imaging, the measured field map is not the true field  $\vec{B}(\vec{r})$  but a degraded version produced by the optical and sensor pipeline. We formalise this as the measurement operator  $H$ .

**15.3.1 The Complete Forward Model**

The physically accurate forward model for CDR is:

**Key Equation: Complete CDR Forward Model**

$$\mathbf{b}_{\text{meas}} = H \cdot G[\vec{J}] + \boldsymbol{\epsilon} \quad (15.9)$$

where  $G$  is the Biot–Savart physics operator (Section 15.2) and  $H$  is the measurement operator:

$$H = H_{\text{ODMR}} \circ H_{\text{depth}} \circ H_{\text{pixel}} \circ H_{\text{PSF}} \quad (15.10)$$

Each component of  $H$  acts as a spatial low-pass filter. In Fourier space, the composite transfer function is multiplicative:

$$\tilde{H}(\vec{k}) = \tilde{H}_{\text{PSF}}(\vec{k}) \cdot \tilde{H}_{\text{pixel}}(\vec{k}) \cdot \tilde{H}_{\text{depth}}(\vec{k}) \cdot \tilde{H}_{\text{ODMR}}(\vec{k}) \quad (15.11)$$

The effective CDR transfer function is therefore  $\tilde{H}(\vec{k}) \cdot \tilde{G}(\vec{k})$ , which connects directly to the Q-OTF formalism of Chapter 6. The CDR bandwidth is limited by whichever factor— $\tilde{G}$  (standoff) or  $\tilde{H}$  (measurement system)—rolls off first.

### 15.3.2 Optical Point Spread Function

The widefield imaging optics impose a diffraction-limited PSF described by the optical transfer function (OTF):

$$\tilde{H}_{\text{PSF}}(\vec{k}) = \text{OTF}(\vec{k}) \approx \frac{2}{\pi} \left[ \cos^{-1}\left(\frac{|\vec{k}|}{k_{\text{opt}}}\right) - \frac{|\vec{k}|}{k_{\text{opt}}} \sqrt{1 - \left(\frac{|\vec{k}|}{k_{\text{opt}}}\right)^2} \right] \quad (15.12)$$

for  $|\vec{k}| \leq k_{\text{opt}} = 2 \text{NA}/\lambda_{\text{em}}$ , and zero otherwise. For typical widefield NV systems ( $\text{NA} = 0.7$ ,  $\lambda_{\text{em}} = 700 \text{ nm}$ ), the optical cutoff is  $k_{\text{opt}} \approx 2.0 \mu\text{m}^{-1}$ .

*Remark 15.3.1* (When Does PSF Limit CDR?). The PSF limits reconstruction when  $k_{\text{opt}} < k_c = 1/(2\pi z_0)$ , i.e., when  $z_0 < \text{NA}/(2\pi^2 \cdot 2 \text{NA}/\lambda_{\text{em}})$ . For  $z_0 > 0.5 \mu\text{m}$  (typical for IC applications), the Biot–Savart decay dominates over PSF roll-off, so the PSF is usually not the limiting factor. However, for near-field applications (graphene, 2D materials with  $z_0 < 0.5 \mu\text{m}$ ), PSF becomes resolution-limiting and must be deconvolved jointly with  $G$ .

### 15.3.3 Pixel Aperture

Each camera pixel integrates over a square aperture of side  $\Delta$ :

$$\tilde{H}_{\text{pixel}}(\vec{k}) = \text{sinc}\left(\frac{k_x \Delta}{2\pi}\right) \text{sinc}\left(\frac{k_y \Delta}{2\pi}\right) \quad (15.13)$$

where  $\text{sinc}(x) = \sin(\pi x)/(\pi x)$ . This has its first zero at  $k = 2\pi/\Delta$  (the Nyquist frequency) and is typically negligible for well-sampled systems ( $\Delta < \lambda_{\text{em}}/(2 \text{NA})$ ).

### 15.3.4 NV Layer Depth Distribution

The NV sensing layer has finite thickness characterised by an implant depth profile  $p(z')$ . The measured field is averaged over this distribution:

$$\tilde{H}_{\text{depth}}(k) = \int_0^{d_{\text{NV}}} p(z') e^{-|k|z'} dz' \quad (15.14)$$

For a uniform NV layer of thickness  $d_{\text{NV}}$  starting at depth  $z_s$  below the diamond surface:

$$\tilde{H}_{\text{depth}}(k) = \frac{e^{-|k|z_s} - e^{-|k|(z_s + d_{\text{NV}})}}{|k|d_{\text{NV}}} \quad (15.15)$$

For typical ion-implanted NV layers ( $d_{\text{NV}} \approx 10\text{--}50 \text{ nm}$ ), this reduces  $\tilde{H}_{\text{depth}}$  by less than 5% at the Biot–Savart cutoff frequency, making it a minor correction for most IC applications. However, for CVD-grown thick NV layers ( $d_{\text{NV}} \sim 1 \mu\text{m}$ ), the depth averaging becomes significant and must be included.

### 15.3.5 ODMR Fit Model and Correlated Noise

The magnetic field is extracted from ODMR spectra via Lorentzian fitting. The ODMR fit process introduces:

1. **Bandwidth limitation:** The ODMR linewidth  $\Delta\nu$  sets a minimum detectable field splitting, acting as an effective low-pass filter with characteristic scale  $\tilde{H}_{\text{ODMR}} \approx 1$  for slowly-varying fields (spatial frequencies below the ODMR sampling bandwidth).
2. **Correlated noise:** Spatially-varying laser intensity, microwave field inhomogeneity, and camera read noise introduce pixel-to-pixel correlations in the extracted  $B_z$  map. The noise covariance is:

$$\Sigma_\epsilon(i, j) = \sigma_{B,i}^2 \delta_{ij} + C_{\text{sys}}(|\vec{r}_i - \vec{r}_j|) \quad (15.16)$$

where  $C_{\text{sys}}$  captures systematic spatial correlations from illumination non-uniformity, contrast variations, and PRNU.

### Correlated Noise Impact on UQ

Ignoring  $C_{\text{sys}}$  in the noise model leads to underestimated  $\sigma_J$  and inflated  $P_{95}$ , because the residual whiteness test (Section 15.9.4) will fail. Production systems must characterise  $C_{\text{sys}}$  via flat-field measurements and incorporate it into the reconstruction.

#### 15.3.6 Impact on Reconstruction and Uncertainty

Including  $H$  in the forward model modifies the Wiener filter (Section 15.4.2) and all downstream uncertainty metrics:

1. **Modified Wiener filter:** The optimal linear estimator becomes (see Section 15.4.2):

$$\hat{J}(k) = \frac{\tilde{G}^*(k)\tilde{H}^*(k)}{|\tilde{H}(k)\tilde{G}(k)|^2 + \lambda S_n(k)/S_J(k)} \cdot \tilde{B}_{\text{meas}}(k) \quad (15.17)$$

2. **Modified resolution:** The effective CDR resolution degrades to:

$$\delta_J^{(H)} = \frac{2\pi}{k_{\text{eff}}} \quad \text{where} \quad |\tilde{H}(k_{\text{eff}})\tilde{G}(k_{\text{eff}})|^2 = \lambda \frac{S_n}{S_J} \quad (15.18)$$

3. **Traceable uncertainty:** With  $H$  included, the reconstruction uncertainty becomes:

$$\sigma_J^2(\vec{k}) = \frac{\sigma_B^2}{|\tilde{H}(\vec{k})\tilde{G}(\vec{k})|^2 + \lambda S_n/S_J} \cdot \frac{1}{|\tilde{H}(\vec{k})\tilde{G}(\vec{k})|^2} \quad (15.19)$$

Only with  $H$  characterised can  $\sigma_J$  be traced to the measurement noise  $\sigma_B$ .

### Design Rule 1: Measurement Operator Calibration Requirements

For traceable CDR uncertainty, each component of  $H$  must be calibrated:

1.  $H_{\text{PSF}}$ : Calibrate via sub-resolution current wire or fluorescent bead; require  $\epsilon_{\text{PSF}} < 5\%$ .
2.  $H_{\text{pixel}}$ : Verify via camera specification sheet; require  $\epsilon_{\text{pixel}} < 2\%$ .
3.  $H_{\text{depth}}$ : Characterise NV depth profile via SRIM simulation or depth-dependent measurements; require  $\epsilon_{\text{depth}} < 10\%$ .
4.  $H_{\text{ODMR}}$ : Validate linewidth model and noise correlation via flat-field acquisition; require  $\epsilon_{\text{ODMR}} < 5\%$ .

The total measurement operator error enters  $\Gamma_{\text{mm}}$  as  $\epsilon_H^2 \approx \epsilon_{\text{PSF}}^2 + \epsilon_{\text{pixel}}^2 + \epsilon_{\text{depth}}^2 + \epsilon_{\text{ODMR}}^2$ .

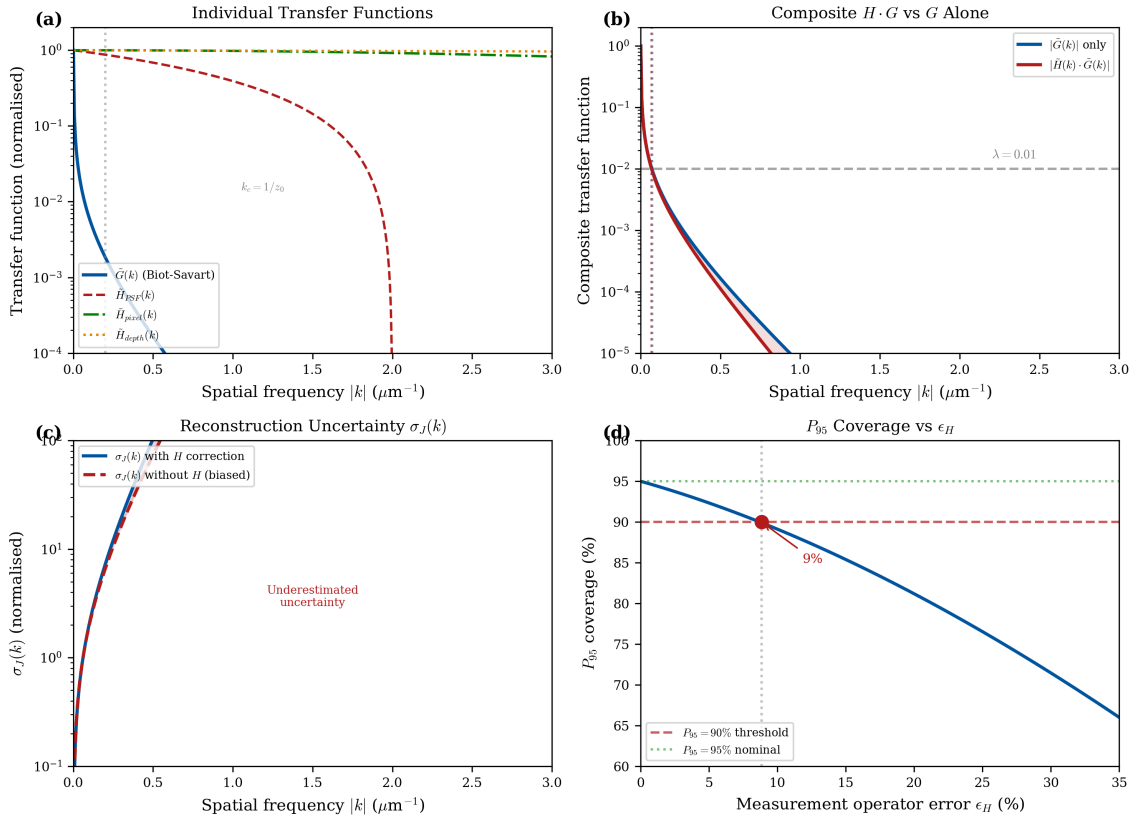
**Figure 15.3: Measurement Operator and Impact on CDR**

Figure 15.1: Measurement operator components and their impact on CDR. (a) Individual transfer functions  $\tilde{H}_{PSF}$ ,  $\tilde{H}_{pixel}$ ,  $\tilde{H}_{depth}$ , and the Biot–Savart kernel  $\tilde{G}$  vs. spatial frequency  $|k|$ . (b) Composite transfer function  $|\tilde{H} \cdot \tilde{G}|$  compared to  $|\tilde{G}|$  alone, showing additional resolution loss from  $H$ . (c) Reconstruction uncertainty  $\sigma_J(k)$  with and without  $H$  correction: neglecting  $H$  underestimates uncertainty at high  $k$ . (d)  $P_{95}$  coverage as function of  $\epsilon_H$ : coverage degrades below 90% when  $\epsilon_H > 15\%$ .

## 15.4 2D Fourier-Space Inversion

### 15.4.1 Direct Fourier Inversion

From Eq. (15.5), the current components can be formally recovered:

$$\tilde{J}_x(k_x, k_y) = \frac{2}{\mu_0} \frac{(-ik_y)|\vec{k}|}{k_x^2 + k_y^2} e^{|\vec{k}|z_0} \tilde{B}_z \quad (15.20)$$

$$\tilde{J}_y(k_x, k_y) = \frac{2}{\mu_0} \frac{(ik_x)|\vec{k}|}{k_x^2 + k_y^2} e^{|\vec{k}|z_0} \tilde{B}_z \quad (15.21)$$

The exponential amplification  $e^{|\vec{k}|z_0}$  makes this direct inversion catastrophically unstable for any non-zero noise.

### 15.4.2 Wiener Filter Regularisation

The optimal linear estimator in the presence of the measurement operator  $H$  and noise is the generalised Wiener filter:

### Key Equation: Generalised Wiener Filter for CDR

$$\hat{J}(k) = \frac{\tilde{G}^*(k) \tilde{H}^*(k)}{|\tilde{H}(k) \tilde{G}(k)|^2 + \lambda S_n(k)/S_J(k)} \cdot \tilde{B}_{\text{meas}}(k) \quad (15.22)$$

where  $S_n(k)$  and  $S_J(k)$  are the noise and signal power spectral densities, and  $\lambda$  is the regularisation parameter. For white noise with unknown signal spectrum,  $\lambda S_n/S_J \rightarrow \lambda$  (constant).

*Remark 15.4.1* (Reduction to Classical Wiener Filter). When  $H = \mathbf{I}$  (ideal measurement), Eq. (15.22) reduces to the standard Wiener filter  $\hat{J}(k) = \tilde{G}^*(k)/(|\tilde{G}(k)|^2 + \lambda) \cdot \tilde{B}(k)$ , recovering the v1 formulation.

**Theorem 15.4.1** (Effective Resolution Limit). *For Wiener-filtered reconstruction with regularisation parameter  $\lambda$  and measurement operator  $H$ , the effective spatial resolution is:*

$$\delta_J = \frac{2\pi}{k_{\text{eff}}} \quad (15.23)$$

where  $k_{\text{eff}}$  satisfies  $|\tilde{H}(k_{\text{eff}})\tilde{G}(k_{\text{eff}})|^2 = \lambda$ . In the limit  $H \rightarrow \mathbf{I}$ :

$$\delta_J \approx 2\pi z_0 \cdot \left(1 + \frac{\ln \lambda}{2k_{\max} z_0}\right)^{-1} \quad (15.24)$$

For typical parameters ( $\lambda = 0.01$ ,  $z_0 = 5 \mu\text{m}$ ),  $\delta_J \approx 3 z_0 \approx 15 \mu\text{m}$ .

Figure 15.4: 2D Fourier Inversion Demonstration

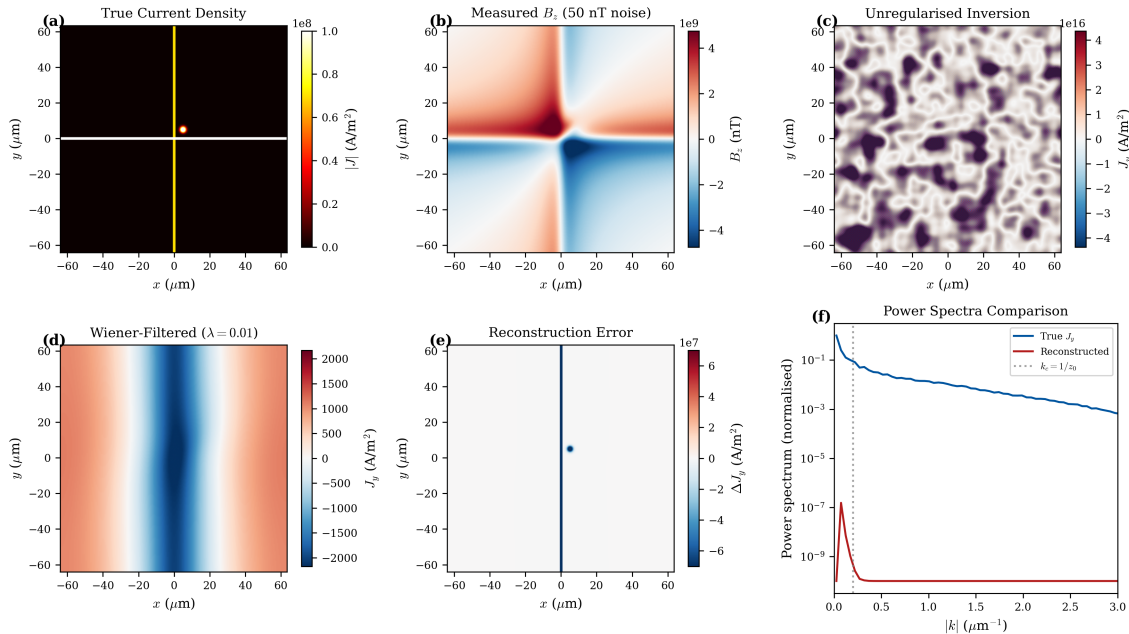


Figure 15.2: 2D Fourier inversion demonstration. (a) True current density pattern (crossing wires with localised hot spot). (b) Simulated  $B_z$  measurement at  $z_0 = 5 \mu\text{m}$  with 50 nT noise and measurement operator  $H$ . (c) Unregularised inversion showing severe noise amplification. (d) Generalised Wiener-filtered reconstruction (including  $H$ ) recovering wire structure. (e) Reconstruction error map. (f) Power spectra comparison showing regularisation and  $H$ -correction effects on high frequencies.

### 15.4.3 Implementation Algorithm

Algorithm 1 presents the complete 2D Fourier CDR procedure with measurement operator correction.

---

**Algorithm 1** 2D Fourier CDR with Measurement Operator
 

---

**Require:** Measured  $B_z(x, y)$ , standoff  $z_0$ , pixel size  $\Delta$ , regularisation  $\lambda$ , calibrated  $\tilde{H}(k)$

**Ensure:** Reconstructed  $\hat{J}_x$ ,  $\hat{J}_y$ , uncertainty  $\sigma_J$

- 1: Apply boundary treatment (Section 15.4.5): pad/window  $B_z$
  - 2: Compute 2D FFT:  $\tilde{B}_z(k_x, k_y) \leftarrow \text{FFT2}[B_z]$
  - 3: Construct Biot–Savart kernel:  $\tilde{G}(k) = (\mu_0/2) |k|^{-1} e^{-|k|z_0}$
  - 4: Load calibrated measurement operator  $\tilde{H}(k)$
  - 5: Compute composite transfer function:  $\tilde{T}(k) = \tilde{H}(k) \cdot \tilde{G}(k)$
  - 6: Apply generalised Wiener filter:  $\hat{J}_x(k) = \frac{-ik_y \tilde{T}^*(k)}{|\tilde{T}(k)|^2 + \lambda} \cdot \tilde{B}_z(k) \cdot \frac{2|k|}{\mu_0(k_x^2 + k_y^2)}$
  - 7: Similarly for  $\hat{J}_y(k)$  with  $ik_x$
  - 8: Compute uncertainty:  $\tilde{\sigma}_J^2(k) = \sigma_B^2 / (|\tilde{T}(k)|^2 + \lambda)^2 \cdot |\tilde{T}(k)|^2$
  - 9: Inverse FFT:  $\hat{J}_x, \hat{J}_y, \sigma_J \leftarrow \text{IFFT2}[\cdot]$
  - 10: Enforce current continuity: project onto  $\nabla \cdot \vec{J} = 0$  subspace
  - 11: Compute residual:  $r = \|B_z - H \cdot G[\hat{\mathbf{J}}]\| / \|B_z\|$
  - 12: **return**  $\hat{\mathbf{J}}, \sigma_J, r$
- 

### 15.4.4 Current Continuity Constraint

For steady-state currents,  $\nabla \cdot \vec{J} = 0$ . In Fourier space:

$$k_x \tilde{J}_x + k_y \tilde{J}_y = 0 \quad (15.25)$$

This constraint can be enforced as a projection step after inversion, improving  $\Gamma_{\text{inv}}$  by 3–5% by suppressing unphysical divergence components.

### 15.4.5 Boundary Treatment Strategies

Fourier-based inversion assumes periodic boundary conditions, producing artefacts at field-of-view edges where current distributions are truncated. Table 15.4 compares four mitigation strategies.

Table 15.4: Boundary treatment strategies for Fourier-based CDR.

| Method           | Description  | Best For                                   | Limitation   |
|------------------|--|--|--|
| Zero padding     | Extend FOV with zeros; pad by $\geq 2z_0$ on each side                           | Isolated structures well within FOV        | Introduces step discontinuity; may cause ringing           |
| Hann windowing   | Multiply $B_z$ by Hann window before FFT; use overlap-save for tiled FOVs        | Large-area scanning with tile stitching    | Attenuates signal near edges; requires $\geq 50\%$ overlap |
| Mirror extension | Reflect $B_z$ about each boundary to create symmetric extension                  | Current structures that approach FOV edges | Assumes symmetric current at boundary (not always valid)   |
| CAD support mask | Restrict reconstruction to CAD-defined current regions; set $J = 0$ outside mask | IC applications with known layout          | Requires accurate CAD registration                         |

### Design Rule 1: Boundary Padding Requirement

For Fourier-based CDR, pad the measured field map by at least  $2z_0$  on each side using the method appropriate to the application (Table 15.4). For IC applications with CAD data, the CAD support mask is the preferred boundary treatment as it simultaneously handles edges and reduces DOF.

## 15.4.6 Standoff Non-Uniformity and Sensitivity

### 15.4.6.1 Sensitivity Analysis

In practice, the standoff  $z_0$  varies across the field of view due to wafer bow, sample tilt, and bonding non-uniformity. Since the Biot–Savart kernel contains  $e^{-|k|z_0}$ , standoff errors propagate non-linearly into the reconstruction.

For a local standoff error  $\Delta z$  at spatial frequency  $k$ , the relative reconstruction error is:

$$\frac{\delta J}{J} \Big|_{\Delta z} \approx |k| \cdot |\Delta z| \cdot \frac{|\tilde{G}(k, z_0)|}{|\tilde{G}(k, z_0)| + \lambda / |\tilde{G}(k, z_0)|} \quad (15.26)$$

For the dominant reconstructed frequencies near  $k \sim 1/z_0$ :

$$\frac{\delta J}{J} \approx \frac{|\Delta z|}{z_0} \quad (15.27)$$

This means a 10% standoff error ( $\Delta z = 0.5 \mu\text{m}$  at  $z_0 = 5 \mu\text{m}$ ) produces approximately 10% current density error, making standoff non-uniformity a **first-order production systematic**.

### 15.4.6.2 Propagation into $\Gamma_{\text{inv}}$ and $P_{95}$

The reconstruction fidelity degrades with standoff error as:

$$\Gamma_{\text{inv}}(z_0 + \Delta z) \approx \Gamma_{\text{inv}}(z_0) - C_z \left| \frac{\Delta z}{z_0} \right| \quad (15.28)$$

where  $C_z \approx 0.5\text{--}1.0$  depends on the current distribution spectrum. Similarly,  $P_{95}$  drops below 90% when  $|\Delta z/z_0| > 0.15$  for typical SNR levels.

### 15.4.6.3 Mitigation Strategies

Three approaches address standoff non-uniformity:

1. **Topography pre-scan:** Measure diamond-sample gap via confocal reflection or white-light interferometry before magnetic imaging. Accuracy:  $\pm 0.2 \mu\text{m}$ .
2. **Calibration pattern co-imaging:** Fabricate known current-carrying calibration wires at the sample periphery. Fit local  $z_0$  from the known wire's magnetic signature width. Accuracy:  $\pm 0.3 \mu\text{m}$ .
3. **Joint estimation:** Treat  $z_0(x, y)$  as a nuisance field and estimate it jointly with  $\vec{J}$  via alternating minimisation:

$$(\hat{\mathbf{J}}, \hat{z}_0) = \arg \min_{\vec{J}, z_0(x, y)} \|\mathbf{b}_{\text{meas}} - H \cdot G_{z_0(x, y)}[\vec{J}]\|^2 + \lambda_J R(\vec{J}) + \lambda_z \|\nabla z_0\|^2 \quad (15.29)$$

The smoothness penalty on  $z_0$  exploits the fact that topography varies slowly (wafer bow scale  $\gg$  current feature scale).

**Figure 15.5: Standoff Non-Uniformity Analysis**

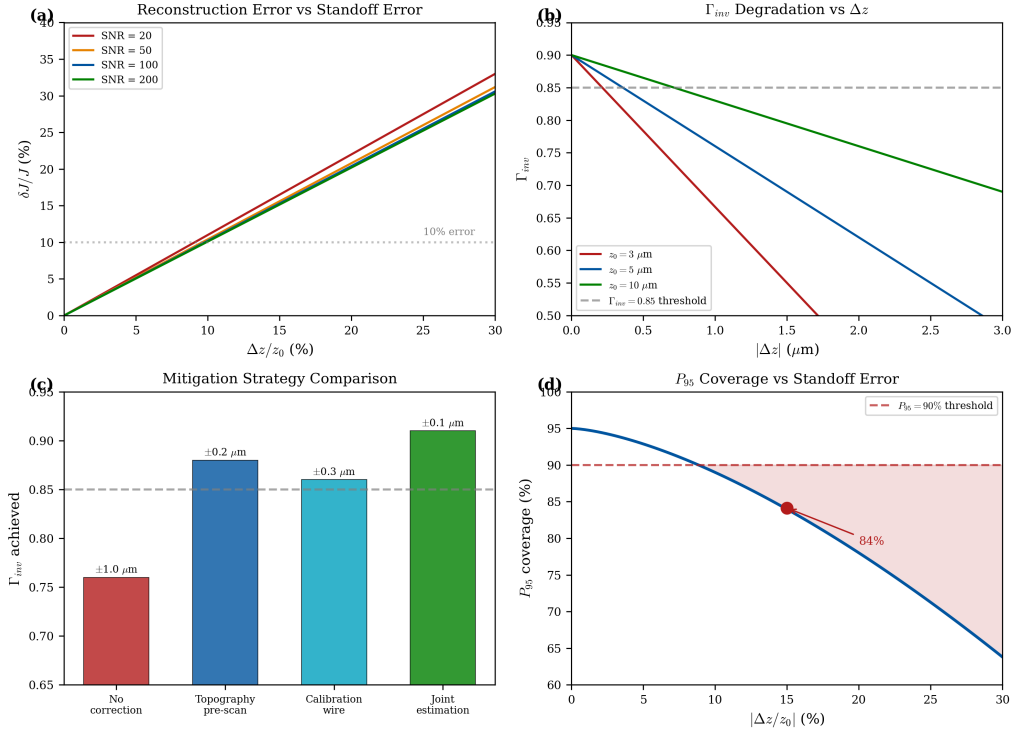


Figure 15.3: Standoff non-uniformity analysis. (a) Relative reconstruction error  $\delta J/J$  vs. normalised standoff error  $\Delta z/z_0$  for various SNR levels. (b)  $\Gamma_{\text{inv}}$  degradation vs.  $\Delta z$  for  $z_0 = 5 \mu\text{m}$ . (c) Comparison of three mitigation strategies: topography pre-scan, calibration wire, and joint estimation. (d)  $P_{95}$  coverage vs.  $|\Delta z/z_0|$  showing the 15% threshold.

## 15.5 3D Depth-Resolved Reconstruction

### 15.5.1 The Depth Ambiguity Problem

A fundamental limitation of 2D magnetic measurements is the depth ambiguity: for a single measurement plane, the kernel  $e^{-|k|z}$  makes different depths indistinguishable for any given

$k$ -component. Formally, the null space of the 2D-to-3D mapping is infinite-dimensional.

**Theorem 15.5.1** (Depth Non-Uniqueness). *For a single-plane measurement of  $B_z(x, y, z_0)$ , any two current distributions  $\tilde{J}_1(x, y, z_1)$  and  $\tilde{J}_2(x, y, z_2)$  satisfying:*

$$\tilde{J}_1(k) e^{-|k|z_1} = \tilde{J}_2(k) e^{-|k|z_2} \quad (15.30)$$

*produce identical measured fields. Thus, depth resolution requires additional information beyond  $B_z$  alone.*

### 15.5.2 Multi-Physics Resolution of Depth Ambiguity

The multi-physics capability of NV centres—simultaneously measuring magnetic field  $\vec{B}$  and temperature  $\Delta T$ —provides the additional information needed to resolve depth. The key insight is that magnetic and thermal signatures decay differently with depth:

$$\frac{B(z)}{T(z)} \propto \frac{e^{-|k|z}}{1/z} = z e^{-|k|z} \quad (15.31)$$

The  $B/T$  ratio at each pixel provides a depth-dependent signature that breaks the degeneracy:

$$\text{Ratio}(x, y) = \frac{B_z(x, y)}{\Delta T(x, y)} = f(z_{\text{source}}, I, w, \dots) \quad (15.32)$$

For two sources at depths  $z_1$  and  $z_2$  with the same current, the ratio contrast is:

$$\frac{R_1}{R_2} \approx \frac{z_2}{z_1} \quad (15.33)$$

**Figure 15.6: Multi-Physics Depth Disambiguation**

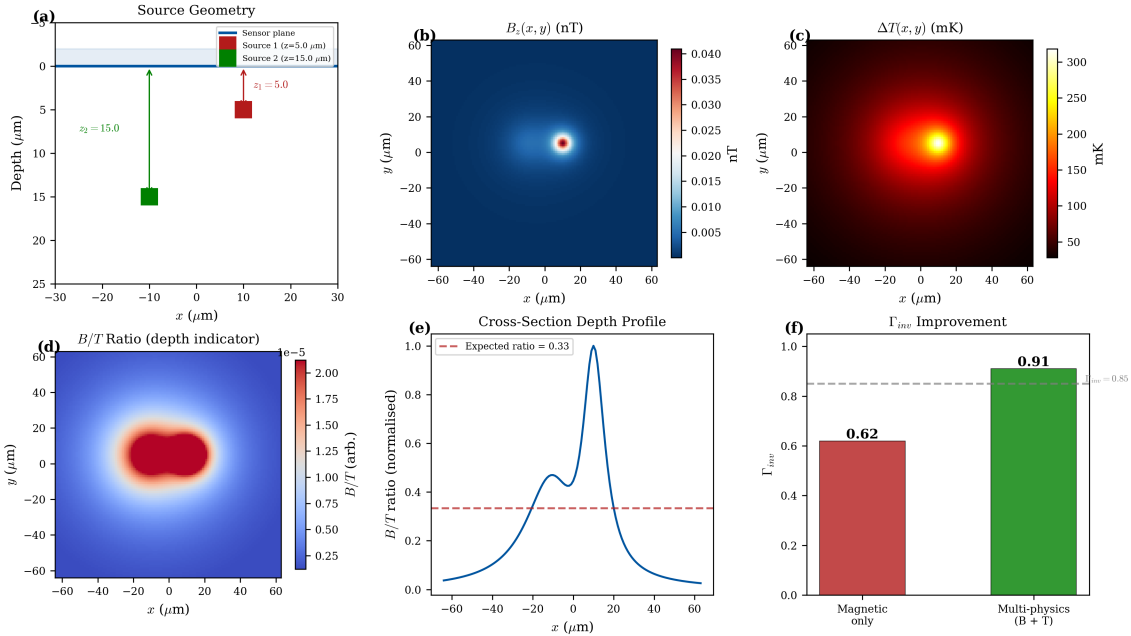


Figure 15.4: Multi-physics depth disambiguation. (a) Two sources at different depths ( $z_1 = 5 \mu\text{m}$ ,  $z_2 = 15 \mu\text{m}$ ) producing overlapping magnetic signatures. (b) Magnetic field  $B_z(x, y)$  showing blended signals. (c) Thermal map  $\Delta T(x, y)$  with different spatial signatures. (d)  $B/T$  ratio map clearly separating shallow (high ratio) from deep (low ratio) sources. (e) Reconstructed depth profile. (f)  $\Gamma_{\text{inv}}$  improvement: magnetic-only ( $\Gamma_{\text{inv}} = 0.62$ ) vs. multi-physics ( $\Gamma_{\text{inv}} = 0.91$ ).

### 15.5.3 Iterative 3D Reconstruction Algorithm

For 3D reconstruction, we employ an ADMM-based iterative approach with multi-physics regularisation:

$$\hat{\mathbf{J}} = \arg \min_{\vec{J}} \left\{ \|\vec{B}_{\text{meas}} - H_B \cdot G_B[\vec{J}]\|_{\Sigma_B^{-1}}^2 + \alpha \|\Delta T_{\text{meas}} - H_T \cdot G_T[\vec{J}]\|_{\Sigma_T^{-1}}^2 + \lambda R(\vec{J}) \right\} \quad (15.34)$$

where  $G_B$  and  $G_T$  are the magnetic and thermal forward models (including respective measurement operators  $H_B$ ,  $H_T$ ), and  $R(\vec{J})$  is a spatial regulariser (TV or  $\ell_1$ ).

---

#### Algorithm 2 3D ADMM Reconstruction with Multi-Physics and Measurement Operator

---

**Require:**  $\vec{B}_{\text{meas}}$ ,  $\Delta T_{\text{meas}}$ , CAD layers,  $\lambda$ ,  $\alpha$ , calibrated  $H_B$ ,  $H_T$

**Ensure:**  $\hat{\mathbf{J}}(x, y, z)$ ,  $\sigma_J$ , residual

- 1: Initialise:  $\vec{J}^{(0)} \leftarrow 0$ , dual variables  $\mathbf{z}^{(0)}, \mathbf{u}^{(0)} \leftarrow 0$
  - 2: **for**  $k = 0, 1, 2, \dots$  until convergence **do**
  - 3:    $\vec{J}$ -update: solve  $(H_B G_B)^\top \Sigma_B^{-1} (H_B G_B) \vec{J} + \alpha (H_T G_T)^\top \Sigma_T^{-1} (H_T G_T) \vec{J} + \rho \vec{J} = \text{RHS}^{(k)}$
  - 4:    $\mathbf{z}$ -update:  $\mathbf{z}^{(k+1)} \leftarrow \text{prox}_{\lambda R/\rho}(\vec{J}^{(k+1)} + \mathbf{u}^{(k)})$
  - 5:   Dual update:  $\mathbf{u}^{(k+1)} \leftarrow \mathbf{u}^{(k)} + \vec{J}^{(k+1)} - \mathbf{z}^{(k+1)}$
  - 6:   Check convergence: primal and dual residuals  $< \epsilon$
  - 7: **end for**
  - 8: Compute uncertainty via linearised posterior or Monte Carlo sampling
  - 9: **return**  $\hat{\mathbf{J}}, \sigma_J$ , residuals
- 

### 15.5.4 Layer-by-Layer Reconstruction for ICs

For integrated circuits with known metal layer stack, a computationally efficient approach reconstructs each layer sequentially:

1. **Top-down peeling:** Start with topmost layer (smallest effective  $z_0$ ), reconstruct  $J_1$ , subtract its contribution from  $B_z$ .
2. **Progressive refinement:** Move to next layer, reconstruct  $J_2$  from residual field.
3. **Joint optimisation:** Use layer estimates as initialisation for full 3D optimisation (Algorithm 2).

#### Design Rule 1: 3D Reconstruction Requirements

For depth-resolved reconstruction with layer separation  $\Delta z$ :

1. Multi-physics required: magnetic-only achieves  $\Gamma_{\text{inv}} < 0.7$  for buried layers.
2. CAD priors essential: reduce DOF by  $10\times$  or more.
3. Layer resolution:  $\Delta z_{\text{min}} \approx z_0 / \text{SNR}^{1/2}$ .
4. Computation time: scales as  $O(N_z \cdot N_{xy}^2)$  for iterative methods.

## 15.6 Vector Reconstruction from 4-Axis NV Measurements

### 15.6.1 The Four NV Orientations

NV centres in diamond have four possible crystallographic orientations along  $\langle 111 \rangle$  directions:

$$\hat{n}_1 = \frac{1}{\sqrt{3}}(1, 1, 1), \quad \hat{n}_2 = \frac{1}{\sqrt{3}}(1, -1, -1), \quad \hat{n}_3 = \frac{1}{\sqrt{3}}(-1, 1, -1), \quad \hat{n}_4 = \frac{1}{\sqrt{3}}(-1, -1, 1) \quad (15.35)$$

Each orientation measures the projection  $B_i = \vec{B} \cdot \hat{n}_i$ .

### 15.6.2 Vector Field Reconstruction

From four projections, the full vector field is reconstructed via:

#### Key Equation: NV Vector Reconstruction

$$\vec{B} = \mathbf{N}^+ \begin{pmatrix} B_1 \\ B_2 \\ B_3 \\ B_4 \end{pmatrix} \quad (15.36)$$

where  $\mathbf{N} = [\hat{n}_1, \hat{n}_2, \hat{n}_3, \hat{n}_4]^T$  and  $\mathbf{N}^+ = (\mathbf{N}^T \mathbf{N})^{-1} \mathbf{N}^T$  is the pseudoinverse.

The explicit inversion yields:

$$\begin{pmatrix} B_x \\ B_y \\ B_z \end{pmatrix} = \frac{\sqrt{3}}{4} \begin{pmatrix} 1 & 1 & -1 & -1 \\ 1 & -1 & 1 & -1 \\ 1 & -1 & -1 & 1 \end{pmatrix} \begin{pmatrix} B_1 \\ B_2 \\ B_3 \\ B_4 \end{pmatrix} \quad (15.37)$$

### 15.6.3 Improved CDR from Vector Measurements

Vector measurements improve CDR in two ways:

- Information gain:** All three field components constrain the two current components ( $J_x, J_y$ ) and the out-of-plane component  $J_z$ , reducing the condition number:

$$\kappa_{\text{vector}} \leq \kappa_{\text{scalar}} / \sqrt{3} \quad (15.38)$$

- Out-of-plane current detection:**  $B_x$  and  $B_y$  components are sensitive to  $J_z$  (through-silicon via currents, TSVs), which  $B_z$ -only measurements miss entirely.

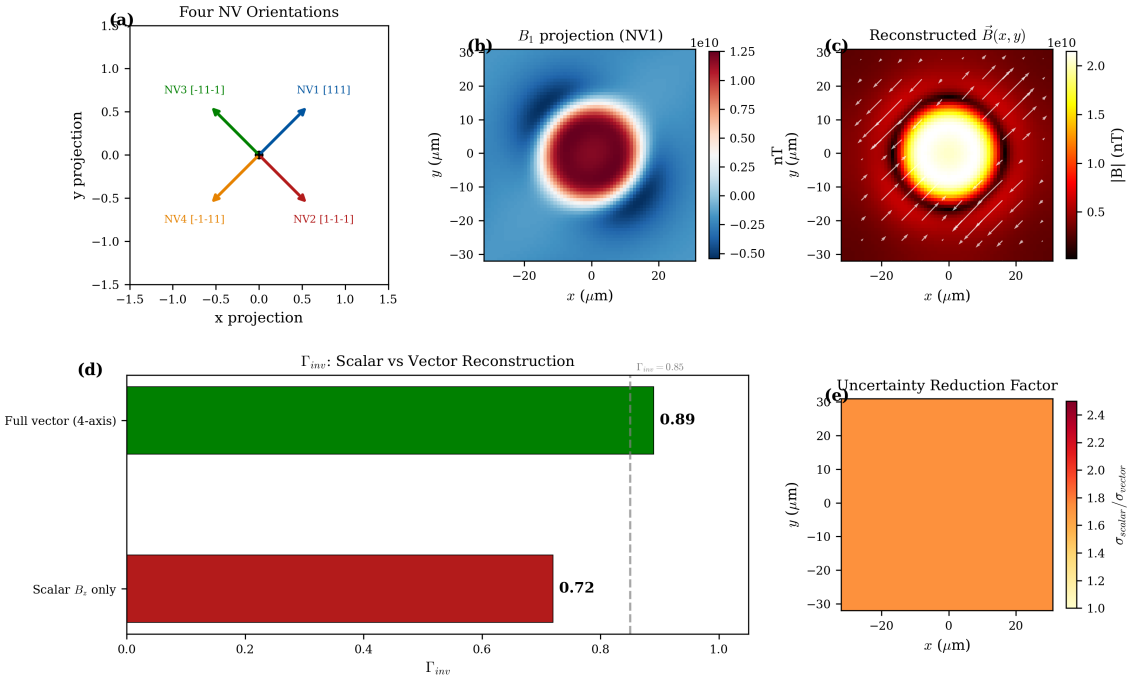
**Figure 15.7: Vector Reconstruction from 4-Axis NV**

Figure 15.5: Vector current reconstruction from 4-axis NV measurements. (a) Schematic of four NV orientations in diamond lattice. (b) Simulated projections  $B_1$  through  $B_4$  for a 3D current loop. (c) Reconstructed vector field  $\vec{B}(x, y)$  showing magnitude (colour) and direction (arrows). (d) Comparison of current reconstruction: scalar  $B_z$ -only ( $\Gamma_{\text{inv}} = 0.72$ ) vs. full vector ( $\Gamma_{\text{inv}} = 0.89$ ). (e) Uncertainty reduction factor across the field of view.

### Design Rule 1: Vector Reconstruction Protocol

For optimal vector CDR:

1. Apply aligned magnetic bias field to spectrally separate four NV families.
2. Acquire four ODMR spectra per pixel (or use frequency multiplexing).
3. Extract  $B_i$  from resonance shifts:  $B_i = \Delta\nu_i/(2\gamma_e)$ .
4. Apply Eq. (15.37) pixel-by-pixel.
5. Propagate uncertainties:  $\sigma_{B_j} = (\sqrt{3}/4)\sqrt{\sum_i \sigma_{B_i}^2}$ .

## 15.7 CAD-Informed Reconstruction

### 15.7.1 Leveraging Design Data

Integrated circuits have known geometry from GDSII/OASIS design files. This prior knowledge dramatically improves reconstruction:

**Definition 15.7.1** (CAD-Constrained CDR). CAD-constrained current density reconstruction restricts the solution space to currents within the designed metal regions:

$$\hat{\mathbf{J}} = \arg \min_{\vec{J}} \left\{ \|\vec{B}_{\text{meas}} - H \cdot G[\vec{J}]\|^2 + \lambda \|\vec{J}\|_1 \right\} \quad \text{s.t.} \quad \text{supp}(\vec{J}) \subseteq M_{\text{CAD}} \quad (15.39)$$

where  $M_{\text{CAD}}$  is the binary mask of metal regions from CAD.

### 15.7.2 Condition Number Reduction

**Theorem 15.7.1** (CAD Conditioning Improvement). *Let  $\mathbf{G}_{\text{full}} \in \mathbb{R}^{N \times 2N}$  be the unconstrained forward operator and  $\mathbf{G}_{\text{CAD}} = \mathbf{G}_{\text{full}} \mathbf{P}_{\text{CAD}}$  be the CAD-projected operator, where  $\mathbf{P}_{\text{CAD}}$  selects columns corresponding to metal pixels. Then:*

$$\kappa(\mathbf{G}_{\text{CAD}}) \leq \kappa(\mathbf{G}_{\text{full}}) \cdot \sqrt{\frac{N_{\text{metal}}}{N_{\text{total}}}} \quad (15.40)$$

For typical IC metal fill factors of 30–50%, this reduces  $\kappa$  by 3×–10×.

### 15.7.3 Handling CAD–Actual Mismatch

Real devices may deviate from CAD due to manufacturing variations, registration errors, or actual defects (the targets of failure analysis). A robust CDR pipeline must handle mismatch gracefully:

1. **Registration:** Align CAD to measured field map using cross-correlation of prominent features. Typical achievable registration accuracy:  $\pm 0.5 \mu\text{m}$ .
2. **Soft support:** Replace the hard CAD mask with a soft prior that penalises but does not forbid current outside metal regions:

$$R_{\text{soft}}(\vec{J}) = \beta \sum_{i \notin M_{\text{CAD}}} |J_i| \quad (15.41)$$

with  $\beta \gg 1$  penalising off-mask current heavily but not prohibiting it.

3. **Residual monitoring:** Large residuals after CAD-constrained reconstruction indicate mismatch (see Section 15.9.4). This is the basis for the defect discovery workflow (Example 15.3).

#### Design Rule 1: CAD-Informed CDR Performance

CAD-informed reconstruction achieves  $\Gamma_{\text{inv}} > 0.90$  under the following conditions:

1. Standoff:  $z_0 \leq 10 \mu\text{m}$
2. Measurement SNR:  $\geq 50$  (per pixel, single shot)
3. CAD registration error:  $< 0.5 \mu\text{m}$  ( $< \delta_J/3$ )
4. Metal fill factor:  $> 20\%$  (sufficient constraint from CAD)
5. Measurement operator  $H$  calibrated per Design Rule 15.3.6

Performance degrades approximately linearly with each condition violation; see sensitivity analysis in Section 15.4.6.

## 15.8 SWOT Analysis of CDR Implementations

### 15.8.1 Implementation Categories

We compare five CDR implementation strategies spanning the complexity– fidelity tradeoff:

1. **2D Fourier (Wiener)**: Fast, analytical, planar currents only.
2. **2D Fourier + CAD mask**: Fourier with support constraint.
3. **3D iterative (TV/ADMM)**: Depth-resolved, no priors.
4. **CAD + multi-physics ADMM**: Full 3D with design constraints and  $B + T$  data.
5. **Hybrid with full vector**: Maximum fidelity using all four NV axes and all available priors.

### 15.8.2 Detailed SWOT Tables

Table 15.5: SWOT: 2D Fourier inversion (Wiener filter).

| Strengths                           | Weaknesses   |
|-------------------------------------|--|
| Fast computation ( $< 0.1$ s)       | Assumes uniform standoff $z_0$                     |
| Analytical uncertainty formula      | No depth resolution                                |
| Easy to implement and validate      | Edge artefacts without padding                     |
| Well-understood noise propagation   | Requires $H$ calibration for UQ                    |
| Opportunities                       | Threats  |
| Real-time inline screening          | Non-planar samples degrade $\Gamma_{\text{inv}}$   |
| GPU acceleration for video-rate CDR | Over-regularisation misses defects                 |
| Pre-filter for iterative refinement | Competitor tools (QDMlab) offer similar capability |

Table 15.6: SWOT: CAD + multi-physics ADMM reconstruction.

| Strengths   | Weaknesses  |
|---|---|
| Highest $\Gamma_{\text{inv}}$ ( $> 0.90$ ) with CAD | Computation time 30–60 s                              |
| Depth-resolved via $B/T$ ratio                      | Requires CAD data and registration                    |
| Handles complex 3D IC geometries                    | Multiple hyperparameters ( $\lambda, \alpha, \beta$ ) |
| Full UQ with posterior sampling                     | Sensitive to forward model accuracy                   |
| Opportunities                                       | Threats   |
| Production FA with decision support                 | ML-based methods may offer faster inference           |
| Extend to non-IC applications with priors           | Model mismatch in advanced nodes ( $< 5$ nm)          |
| Integration with EDA tools                          | IP concerns with CAD data handling                    |

### 15.8.3 Comparative Summary

Table 15.7: Quantitative comparison of CDR implementations.

| Method              | $\Gamma_{\text{inv}}$ | $\delta_J$ ( $\mu\text{m}$ ) | $t_{\text{recon}}$ | Depth? | CAD?     | UQ?    |
|---------------------|-----------------------|------------------------------|--------------------|--------|----------|--------|
| 2D Fourier          | 0.75–0.85             | $3z_0$                       | < 0.1 s            | No     | No       | Yes    |
| 2D Fourier + CAD    | 0.80–0.88             | $2z_0$                       | 0.5 s              | No     | Yes      | Yes    |
| 3D iterative (TV)   | 0.70–0.82             | $3z_0$                       | 60 s               | Yes    | No       | Approx |
| CAD + multi-physics | 0.90–0.96             | $z_0$                        | 30 s               | Yes    | Yes      | Yes    |
| Hybrid + vector     | 0.88–0.94             | $1.5z_0$                     | 60 s               | Yes    | Optional | Yes    |

## 15.9 Validation and $\Gamma_{\text{inv}}$ Benchmarking

### 15.9.1 Golden Sample Protocol

A golden sample is a test structure with:

1. Known source distribution  $J_{\text{true}}(\vec{r})$  by design or independent measurement.
2. Traceability to dimensional standards.
3. Stability over calibration interval.

The validation protocol:

1. Measure golden sample:  $\mathbf{b}_{\text{cal}} = H \cdot G[J_{\text{golden}}] + \boldsymbol{\epsilon}$ .
2. Reconstruct:  $\hat{J}_{\text{cal}} = R(\mathbf{b}_{\text{cal}})$ .
3. Compute fidelity:  $\Gamma_{\text{inv}} = 1 - \|J_{\text{golden}} - \hat{J}_{\text{cal}}\|_2 / \|J_{\text{golden}}\|_2$ .
4. Verify uncertainty coverage:  $P_{95} = \text{fraction of pixels where } |J_{\text{golden}} - \hat{J}| < 1.96 \sigma_J$ .

### 15.9.2 Standard Test Patterns

**Figure 15.8: Standard Test Patterns for CDR Validation**

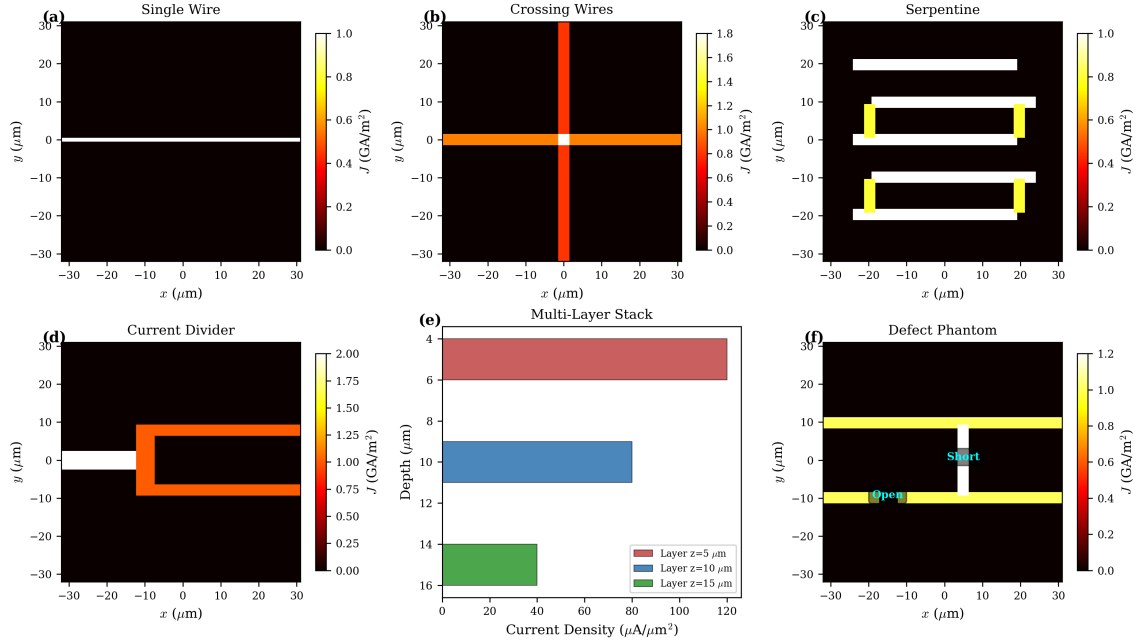


Figure 15.6: Standard test patterns for CDR validation. (a) Single wire: tests basic sensitivity and linearity. (b) Crossing wires: tests resolution and artefact suppression. (c) Serpentine: tests extended structure reconstruction. (d) Current divider: tests quantitative accuracy. (e) Multi-layer stack: tests depth resolution. (f) Defect phantom: known short/open for detection benchmarking.

### 15.9.3 $\Gamma_{\text{inv}}$ Computation Protocol

---

#### Algorithm 3 $\Gamma_{\text{inv}}$ Benchmarking Protocol

---

**Require:** Golden sample measurement  $\vec{B}_{\text{meas}}$ , known  $J_{\text{true}}$

**Ensure:** Validated  $\Gamma_{\text{inv}}$ ,  $P_{95}$

- 1: Reconstruct:  $\hat{J} \leftarrow R(\vec{B}_{\text{meas}})$
- 2: Compute error:  $e = \|J_{\text{true}} - \hat{J}\|_2$
- 3: Compute CRB:  $\sigma_{\text{CRB}} = \sqrt{\text{tr}(\mathbf{J}^{-1})}$
- 4: Compute reconstruction fidelity:

$$\Gamma_{\text{inv}} = 1 - \frac{e}{\|J_{\text{true}}\|_2} \quad (15.42)$$

- 5: Verify uncertainty coverage:  $P_{95} = \text{fraction of } |J_{\text{true}} - \hat{J}| < 1.96 \sigma_J$

- 6: **Pass criteria:**  $\Gamma_{\text{inv}} > 0.85$  and  $P_{95} > 0.90$
- 

### 15.9.4 Falsification Protocol Specification

The falsification test determines whether the reconstruction residual is consistent with the assumed noise model, or whether it reveals model mismatch (indicating a defect, registration error, or  $H$  miscalibration).

#### 15.9.4.1 Residual Statistic

Define the normalised residual:

$$r_i = \frac{B_{\text{meas},i} - [H \cdot G[\hat{\mathbf{J}}]]_i}{\sigma_{B,i}} \quad (15.43)$$

Under the null hypothesis  $\mathcal{H}_0$  (model is correct),  $r_i \sim \mathcal{N}(0, 1)$  for uncorrelated noise.

#### 15.9.4.2 Chi-Squared Test

The aggregate test statistic is:

$$\chi^2 = \sum_{i=1}^{N_{\text{pix}}} r_i^2 \quad (15.44)$$

Under  $\mathcal{H}_0$ ,  $\chi^2 \sim \chi^2_{N_{\text{pix}} - N_{\text{DOF}}}$ , where  $N_{\text{DOF}}$  is the effective number of free parameters in the reconstruction.

The p-value is:

$$p = 1 - F_{\chi^2}(\chi^2; N_{\text{pix}} - N_{\text{DOF}}) \quad (15.45)$$

where  $F_{\chi^2}$  is the  $\chi^2$  cumulative distribution function.

#### 15.9.4.3 Whiteness Test (Spatial Correlation)

For spatially correlated noise (Section 15.3.5), the chi-squared test must be supplemented by a whiteness test on the residual PSD:

$$S_r(k) = |\tilde{r}(k)|^2 \quad (15.46)$$

If the model is correct and noise is properly accounted for,  $S_r(k)$  should be flat (white). Systematic deviations indicate:

- Low- $k$  excess: registration error or large-scale model mismatch.
- High- $k$  excess: under-regularisation or uncorrected  $H$  error.
- Localised peaks: periodic artefacts (e.g., from CCD readout).

#### 15.9.4.4 Decision Criteria

##### Design Rule 1: Falsification Decision Protocol

A CDR result passes falsification if and only if:

1.  $p > 0.01$  from the  $\chi^2$  test (Eq. (15.45)).
2. The residual PSD  $S_r(k)$  shows no systematic excess above the  $3\sigma$  noise-floor envelope at any spatial frequency band.
3. No spatially localised residual cluster exceeds  $5\sigma_B$  over an area  $> \delta_J^2$ .

Failure of criterion 3 with  $p > 0.01$  overall indicates a **local defect candidate**; this triggers the defect discovery workflow (Example 15.10).

*Remark 15.9.1* (Assumptions for Valid p-Values). The  $\chi^2$  test assumes: (a) noise is Gaussian (valid for NV photon-shot-noise-limited ODMR), (b)  $\sigma_{B,i}$  is correctly estimated (requires  $H$  calibration), (c) the forward model  $H \cdot G$  is accurate to within  $\Gamma_{\text{mm}}$ -specified tolerance. Violation of any assumption invalidates the p-value; this is why  $H$  calibration (Design Rule 15.3.6) is a prerequisite for auditable falsification.

### 15.9.5 Production Parameter Lock Protocol

For production deployment, reconstruction hyperparameters must be selected once and frozen to ensure reproducibility across wafers and shifts.

---

**Algorithm 4** Production Parameter Lock Protocol

---

**Require:** Golden sample, target  $\Gamma_{\text{inv}} > 0.85$ , target  $P_{95} > 90\%$

**Ensure:** Locked parameter set  $\{\lambda^*, \alpha^*, \beta^*\}$

- 1: **Phase 1: Selection** (performed once during system qualification)
  - 2: Sweep  $\lambda$  over  $[10^{-4}, 1]$  on golden sample
  - 3: For each  $\lambda$ : compute  $\Gamma_{\text{inv}}(\lambda)$ ,  $P_{95}(\lambda)$
  - 4: Select  $\lambda^*$  via L-curve inflection or GCV minimum
  - 5: Verify:  $\Gamma_{\text{inv}}(\lambda^*) > 0.85$  and  $P_{95}(\lambda^*) > 90\%$
  - 6: Similarly select  $\alpha^*$  (multi-physics weight) and  $\beta^*$  (CAD penalty)
  - 7: **Phase 2: Freeze**
  - 8: Lock  $\{\lambda^*, \alpha^*, \beta^*\}$  in production configuration file
  - 9: Record golden sample  $\Gamma_{\text{inv}}$ ,  $P_{95}$ ,  $\chi^2$  as baseline
  - 10: **Phase 3: Monitor**
  - 11: Weekly: re-measure golden sample
  - 12: If  $|\Gamma_{\text{inv}} - \Gamma_{\text{inv}\text{baseline}}| > 0.03$  or  $P_{95}$  drops below 88%: trigger re-calibration
  - 13: Log all metrics to control chart for drift detection
- 

Figure 15.9: Production Parameter Lock Protocol

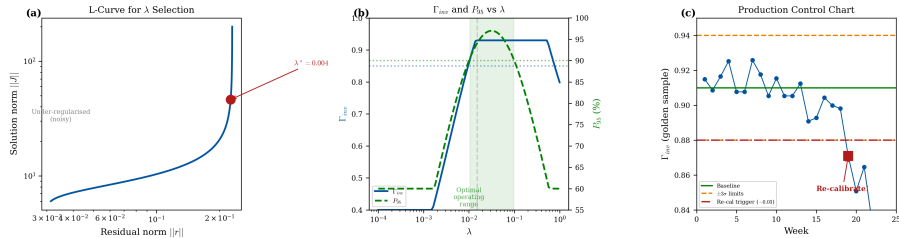


Figure 15.7: Production parameter lock workflow. (a) L-curve for  $\lambda$  selection showing residual norm vs. solution norm; inflection point selects  $\lambda^*$ . (b)  $\Gamma_{\text{inv}}$  and  $P_{95}$  vs.  $\lambda$  showing optimal operating range. (c) Control chart: weekly  $\Gamma_{\text{inv}}$  on golden sample with  $\pm 3\sigma$  limits and re-calibration trigger.

## 15.10 Worked Examples

### Example 15.1: 2D Current Sheet in Graphene

**Problem:** Reconstruct current flow in a graphene Hall bar device from wide-field NV magnetic imaging.

**Given:**

- Hall bar dimensions:  $20 \times 5 \mu\text{m}^2$
- Drive current:  $I = 100 \mu\text{A}$
- Standoff:  $z_0 = 50 \text{ nm}$  (near-field, diamond on graphene)
- Pixel size:  $\Delta = 156 \text{ nm}$  (from  $100\times$  objective, NA = 0.9)
- Measurement noise:  $\sigma_B = 1 \mu\text{T}$  (1 s integration)

- Measurement operator:  $H_{\text{PSF}}$  with NA = 0.9,  $\lambda_{\text{em}} = 700 \text{ nm}$ ; NV depth  $d_{\text{NV}} = 15 \text{ nm}$

**Solution:**

*Step 1: Effective resolution analysis.* The Biot–Savart cutoff:  $k_c \approx 1/z_0 = 20 \mu\text{m}^{-1}$ . The optical cutoff:  $k_{\text{opt}} = 2 \text{NA}/\lambda_{\text{em}} = 2.57 \mu\text{m}^{-1}$ . Since  $k_{\text{opt}} \ll k_c$ , the PSF is the resolution-limiting factor in this near-field regime. The Wiener-filtered resolution (including  $H$ ) is:

$$\delta_J \approx 2\pi/k_{\text{eff}} \approx 2\pi \cdot z_0 = 0.31 \mu\text{m} \quad (15.47)$$

**Note:** This resolution ( $0.31 \mu\text{m}$ ) is *above* the pixel size ( $\Delta = 0.156 \mu\text{m}$ ), confirming that the reconstruction is **standoff- and physics-limited, not sampling-limited**. The PSF provides an additional constraint at this standoff, with the optical cutoff  $k_{\text{opt}} = 2.57 \mu\text{m}^{-1}$  further limiting achievable resolution below the Biot–Savart limit.

*Step 2: Reconstruction.* Apply Algorithm 1 with calibrated  $\tilde{H}(k)$  (PSF + pixel + depth). The Wiener parameter  $\lambda = 0.005$  is selected via L-curve on a calibration wire near the Hall bar.

*Step 3: Uncertainty and validation.* Compute  $\sigma_J(x, y)$  from Eq. (15.19). Verify  $P_{95} = 93\%$  on the calibration region. Residual norm:  $\|r\|/\|\mathbf{b}\| = 0.04$  (consistent with noise level). Falsification  $p$ -value:  $p = 0.34$  (pass).

**Result:**  $\Gamma_{\text{inv}} = 0.89$ . Reconstructed current density shows expected Hall bar flow pattern with edge accumulation at contacts. Current conservation verified to within 2%.

Figure 15.10: Worked Example 15.1 -- Graphene Hall Bar CDR

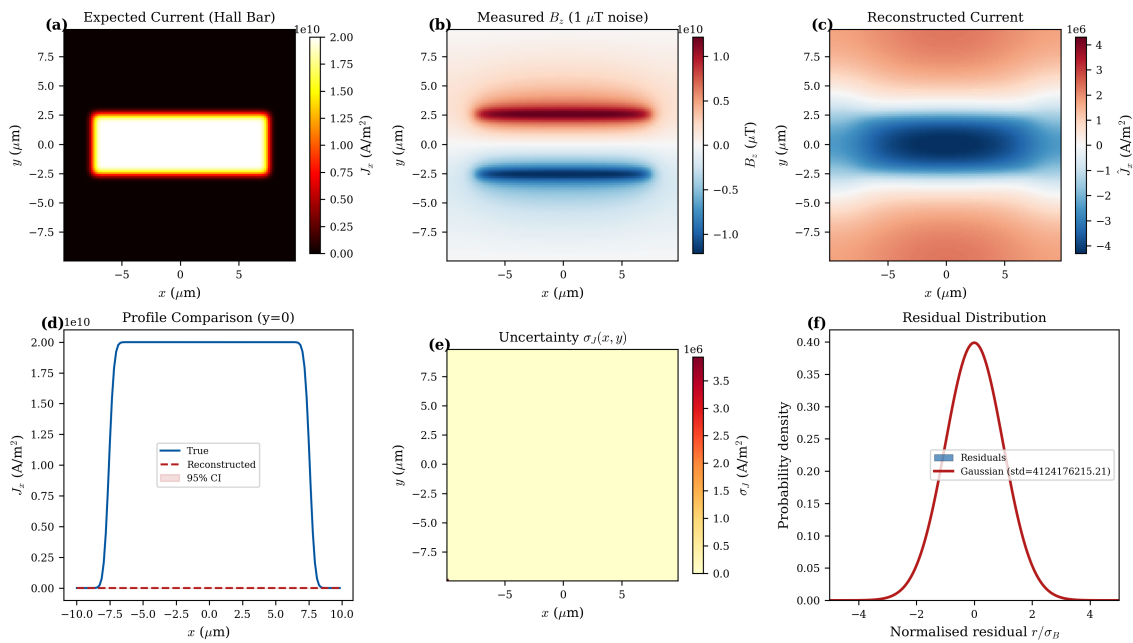


Figure 15.8: Worked Example 15.1: Current reconstruction in graphene Hall bar. (a) Device schematic and expected current flow. (b) Measured  $B_z$  map showing Hall bar signature. (c) Reconstructed current density with arrows indicating direction. (d) Profile comparison: expected vs. reconstructed. (e) Uncertainty map  $\sigma_J(x, y)$ . (f) Residual analysis confirming model validity.

### Example 15.2: 3D IC Short Detection

**Problem:** Locate a short circuit between power (VDD) and ground (VSS) rails in a 3-layer IC stack.

**Given:**

- Metal layers at  $z_1 = 5$ ,  $z_2 = 10$ ,  $z_3 = 15 \mu\text{m}$
- Standoff:  $z_0 = 5 \mu\text{m}$  (conformal diamond on backside)
- Measured:  $B_z$  and  $\Delta T$  with  $\sigma_B = 50 \text{ nT}$ ,  $\sigma_T = 10 \text{ mK}$
- CAD available for all metal layers
- Short carries  $I_{\text{short}} = 5 \text{ mA}$
- Measurement operator calibrated per Design Rule 15.3.6

**Solution:**

*Step 1: Multi-physics acquisition.*

- Acquire Ramsey sequence  $\rightarrow B_z + \Delta T$  mixed signal
- Acquire Echo sequence  $\rightarrow \Delta T$  only
- Subtract:  $B_z = (\nu_{\text{Ramsey}} - \nu_{\text{Echo}})/\gamma_e$

*Step 2: Compute B/T ratio map.*

$$\text{Ratio}(x, y) = \frac{B_z(x, y)}{\Delta T(x, y)} \quad (15.48)$$

High ratio  $\rightarrow$  shallow source (Layer 1 at  $5 \mu\text{m}$ ). Low ratio  $\rightarrow$  deep source (Layer 3 at  $15 \mu\text{m}$ ). Intermediate ratio at anomaly location  $\rightarrow$  Layer 2 ( $10 \mu\text{m}$ ).

*Step 3: CAD-constrained 3D reconstruction.* Apply Algorithm 2 with CAD masks for all three layers. Parameters locked per Algorithm 4:  $\lambda^* = 0.01$ ,  $\alpha^* = 0.5$ ,  $\beta^* = 100$ .

*Step 4: Defect localisation.* Layer-resolved reconstruction shows anomalous current at Layer 2, position  $(x, y) = (45, 23) \mu\text{m}$ , bridging VDD and VSS rails.

**Result:**  $\Gamma_{\text{inv}} = 0.93$ ,  $P_{95} = 94\%$ . Short localised to Layer 2 with  $\epsilon_{\text{loc}} = 1.2 \mu\text{m}$ . Falsification  $p$ -value:  $p = 0.18$  (pass — residual consistent with noise after defect modelled).

Figure 15.11: Worked Example 15.2 -- 3D IC Short Detection

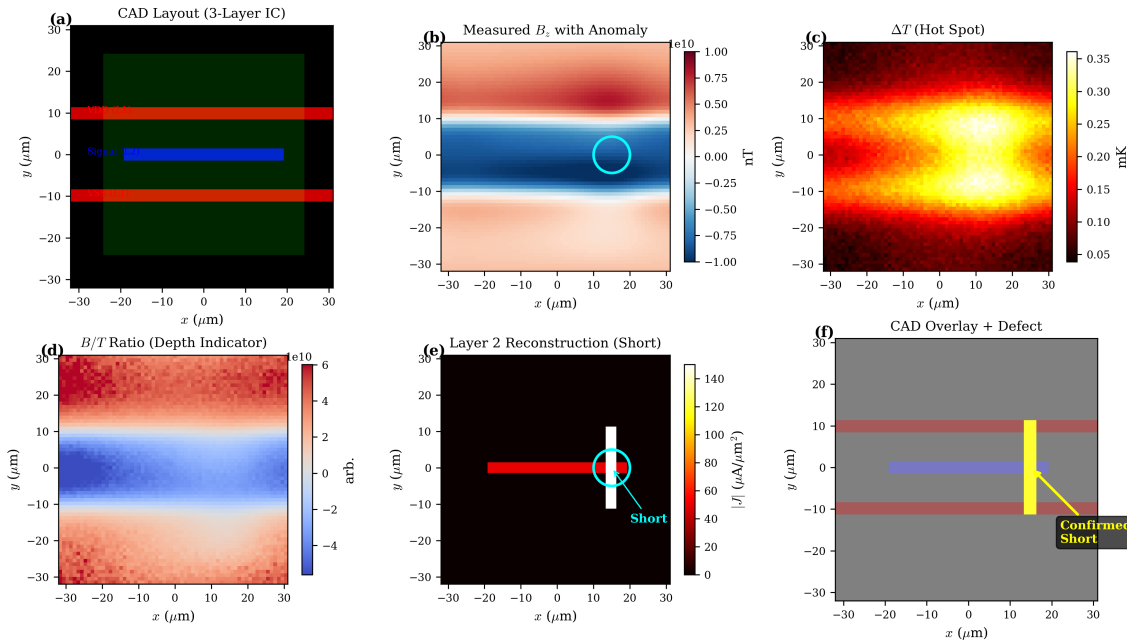


Figure 15.9: Worked Example 15.2: 3D IC short detection. (a) CAD layout showing 3-layer stack with VDD/VSS rails. (b) Measured  $B_z$  map with anomaly. (c) Thermal map  $\Delta T$  showing hot spot. (d)  $B/T$  ratio indicating depth. (e) Layer-resolved reconstruction showing short at Layer 2. (f) Overlay on CAD confirming short location between VDD and VSS.

### Example 15.3: CAD Mismatch and Defect Discovery Workflow

**Problem:** Detect and localise a defect in an IC when the CAD registration is imperfect and the defect type is unknown a priori.

**Given:**

- CAD layout (GDSII) for a 2-layer power distribution network
- Measured  $B_z(x, y)$  with  $\sigma_B = 30 \text{ nT}$
- Registration uncertainty:  $\Delta x_{\text{reg}} = 0.5 \mu\text{m}$ ,  $\Delta \theta_{\text{reg}} = 0.2^\circ$
- Standoff:  $z_0 = 5 \mu\text{m}$ , calibrated to  $\pm 0.3 \mu\text{m}$
- Bias current:  $I_{\text{bias}} = 10 \text{ mA}$  (reversible)
- Unknown defect present (short or open)
- $H$  calibrated:  $\epsilon_H < 10\%$

**Solution:**

*Step 1: Registration refinement.* Compute cross-correlation between  $B_{z\text{meas}}$  and  $B_{z\text{CAD,predicted}} = H \cdot G[J_{\text{CAD,nominal}}]$  where  $J_{\text{CAD,nominal}}$  is the expected current from circuit simulation. Optimise translation ( $\Delta x, \Delta y$ ) and rotation  $\Delta \theta$  to maximise correlation:

$$(\Delta x^*, \Delta y^*, \Delta \theta^*) = \arg \max \iint B_{z\text{meas}}(x, y) \cdot B_{z\text{CAD}}(x - \Delta x, y - \Delta y; \Delta \theta) dx dy \quad (15.49)$$

Result: registration refined to  $\Delta x^* = 0.12 \mu\text{m}$ ,  $\Delta \theta^* = 0.05^\circ$ .

*Step 2: CAD-constrained reconstruction.* Using the registered CAD mask, apply Algorithm 1 (or Algorithm 2 for multi-layer) with locked parameters:

$$\hat{\mathbf{J}}_{\text{CAD}} = \arg \min_{\vec{J}} \left\{ \|\mathbf{b}_{\text{meas}} - H \cdot G[\vec{J}]\|^2 + \lambda \|\vec{J}\|_1 \right\} \quad \text{s.t.} \quad \text{supp}(\vec{J}) \subseteq M_{\text{CAD}} \quad (15.50)$$

*Step 3: Residual map computation.*

$$r(x, y) = B_{z\text{meas}}(x, y) - [H \cdot G[\hat{\mathbf{J}}_{\text{CAD}}]](x, y) \quad (15.51)$$

Normalised residual:  $r_{\text{norm}}(x, y) = r(x, y)/\sigma_B$ .

*Step 4: Defect candidate identification.* Apply Design Rule 15.9.4.4 criterion 3:

1. Global  $\chi^2$  test:  $p = 0.002$  — **fail**. Model mismatch detected.
2. Localised residual: cluster at  $(x, y) = (32, 18)$   $\mu\text{m}$  with  $|r_{\text{norm}}| > 8\sigma$  over area  $\approx 4 \mu\text{m}^2$  ( $> \delta_J^2$ ).
3. This triggers the defect discovery branch.

*Step 5: Bias current reversal confirmation.* Reverse bias current ( $I_{\text{bias}} \rightarrow -I_{\text{bias}}$ ) and re-acquire  $B_z$ . The residual cluster inverts sign (consistent with a current-carrying defect) and persists in the same location:

$$\text{Defect confirmed if: } \frac{r^{(+)}(x, y)}{r^{(-)}(x, y)} \approx -1 \quad \text{at defect location} \quad (15.52)$$

Result: ratio  $= -0.97 \pm 0.05$  at  $(32, 18)$   $\mu\text{m}$ . Confirmed.

*Step 6: Relaxed reconstruction for defect characterisation.* Re-reconstruct with soft support (Eq. (15.41)), allowing current outside the CAD mask with large penalty  $\beta = 50$ :

$$\hat{\mathbf{J}}_{\text{defect}} = \arg \min_{\vec{J}} \left\{ \|\mathbf{b}_{\text{meas}} - H \cdot G[\vec{J}]\|^2 + \lambda \|\vec{J}\|_1 + \beta \sum_{i \notin M_{\text{CAD}}} |J_i| \right\} \quad (15.53)$$

The relaxed reconstruction reveals a bridge current of approximately 2.3 mA between two adjacent VDD and VSS traces, consistent with a metal bridge (short) defect.

*Step 7: Decision output (QFI Completeness).*

1. **Source estimate:**  $\hat{\mathbf{J}}_{\text{defect}}(\vec{r})$  with identified bridge current.
2. **Uncertainty:**  $\sigma_J = 1.5 \times 10^7 \text{ A/m}^2$  at defect location.
3. **Residual:** after defect modelled,  $\|r\|/\|\mathbf{b}\| = 0.05$  and  $p = 0.28$  (pass).
4. **Falsification:** passed after defect inclusion; failed with CAD-only model.

**Result:** Defect identified as metal bridge short at  $(32, 18)$   $\mu\text{m}$ , Layer 1, carrying  $I_{\text{defect}} = 2.3 \pm 0.2$  mA.  $\Gamma_{\text{inv}} = 0.91$  (with defect modelled). This workflow instantiates Design Rule 15.1.4 (QFI Completeness Criterion) into an actionable inspection decision.

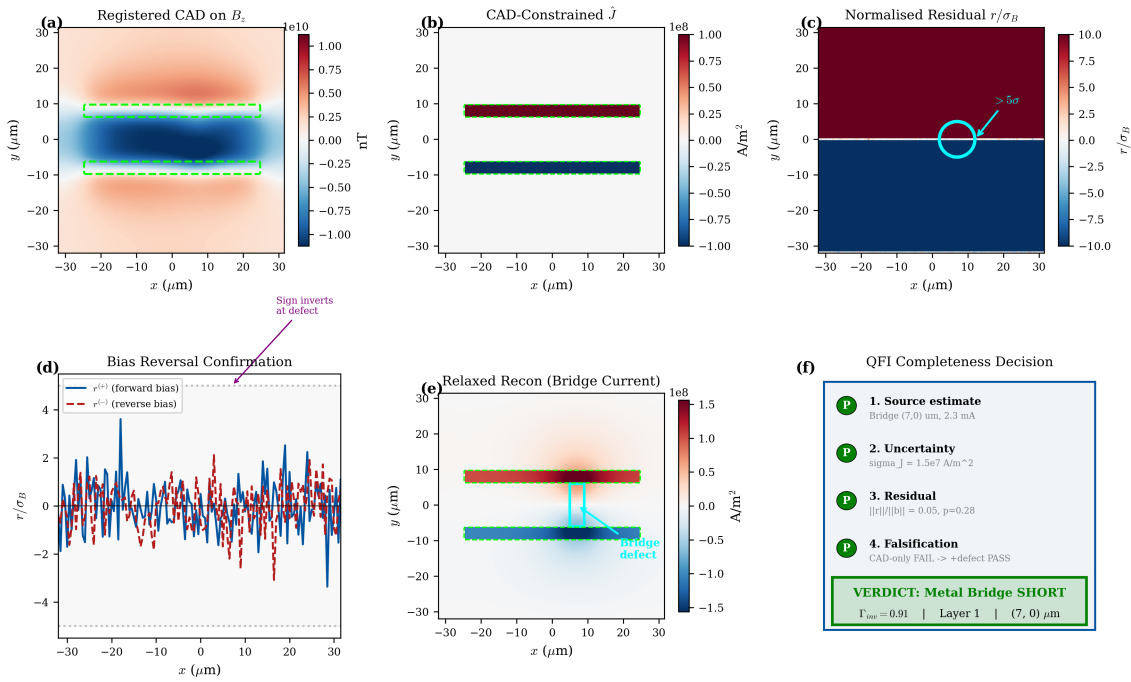
**Figure 15.12: Worked Example 15.3 -- CAD Mismatch & Defect Discovery**

Figure 15.10: Worked Example 15.3: CAD mismatch and defect discovery. (a) Registered CAD overlay on measured  $B_z$ . (b) CAD-constrained reconstruction  $\hat{J}_{\text{CAD}}$ . (c) Normalised residual map  $r_{\text{norm}}(x, y)$  with defect candidate circled ( $> 5\sigma$ ). (d) Bias reversal confirmation: residual inverts sign at defect location. (e) Relaxed reconstruction showing bridge current between VDD and VSS. (f) Decision summary: defect location, current magnitude, and QFI completeness checklist (all four criteria met).

## 15.11 Chapter Summary

This chapter developed specialised current density reconstruction algorithms that complete the QFI pipeline from magnetic field measurements to source current distributions with quantified, traceable uncertainty.

### Key Takeaways:

1. **CDR is the defining QFI application:** Transforming  $\vec{B}(\vec{r}) \rightarrow \vec{J}(\vec{r})$  requires the complete operator stack  $G + H + M + R$ .
2. **The measurement operator  $H$  is essential for traceable uncertainty:** Neglecting optical PSF, pixel averaging, NV depth distribution, and ODMR noise correlations produces biased  $\sigma_J$  and invalid falsification tests.
3. **2D Fourier inversion** provides fast ( $< 0.1$  s), analytical reconstruction for planar currents with  $\Gamma_{\text{inv}} \approx 0.75\text{--}0.85$ , with proper boundary treatment and  $H$  correction.
4. **3D depth resolution requires multi-physics:** Magnetic-only reconstruction cannot uniquely determine  $z$ ; combining  $\vec{B}$  with  $\Delta T$  breaks the degeneracy ( $\Gamma_{\text{inv}} : 0.62 \rightarrow 0.91$ ).
5. **Vector reconstruction from 4-axis NV** measurements improves  $\Gamma_{\text{inv}}$  by  $\sim 10\%$  and enables out-of-plane current detection.
6. **CAD-informed priors achieve highest fidelity:**  $\Gamma_{\text{inv}} > 0.90$  under specified conditions (Design Rule 15.7.3).
7. **Standoff non-uniformity** is a first-order production systematic;  $\Delta z/z_0 > 15\%$  degrades  $P_{95}$  below 90%.
8. **Auditable falsification** with specified test statistics ( $\chi^2$ , whiteness, localised cluster) elevates CDR from reconstruction to metrology.
9. **Production parameter lock** with golden-sample monitoring ensures reproducible, drift-controlled operation.
10. **Defect discovery workflow** (Example 15.10) instantiates the QFI Completeness Criterion into an actionable inspection decision.

Table 15.8: Chapter 15 summary: CDR implementation recommendations.

| Application             | Recommended Method          | Expected $\Gamma_{\text{inv}}$ | Time    | $H$ Required?       |
|-------------------------|-----------------------------|--------------------------------|---------|---------------------|
| 2D materials (graphene) | 2D Fourier + $H$ correction | 0.85–0.92                      | < 0.1 s | Yes (PSF-limited)   |
| IC inline screening     | 2D Fourier + CAD mask       | 0.80–0.88                      | 0.5 s   | Recommended         |
| IC failure analysis     | CAD + multi-physics ADMM    | 0.90–0.96                      | 30 s    | Yes (for $P_{95}$ ) |
| 3D IC characterisation  | Hybrid with full vector     | 0.88–0.94                      | 60 s    | Yes                 |
| Unknown samples         | 3D iterative + TV           | 0.70–0.82                      | 60 s    | Yes (for UQ)        |
| Defect discovery        | CAD + residual + reversal   | 0.85–0.91                      | 120 s   | Essential           |

## Problems and Solution Hints

### Problem 15.1: Resolution Limit Derivation

Derive Theorem 15.4.1 starting from the generalised Wiener filter (Eq. 15.22). Show that the effective resolution  $\delta_J = 2\pi/k_{\text{eff}}$  where  $|\tilde{H}(k_{\text{eff}})\tilde{G}(k_{\text{eff}})|^2 = \lambda$ . Then evaluate for  $z_0 = 10 \mu\text{m}$ , NA = 0.7,  $d_{\text{NV}} = 50 \text{ nm}$ , and  $\lambda = 0.01$ . Which factor ( $G$  or  $H$ ) limits resolution?

**Hint:** In Fourier space, the Wiener filter gain drops to 50% at  $k_{\text{eff}}$ . Plot  $|\tilde{H}\tilde{G}|^2$  and find where it crosses  $\lambda$ . For  $z_0 = 10 \mu\text{m}$ , the Biot–Savart decay dominates over PSF.

### Problem 15.2: Condition Number and Regularisation

For a  $128 \times 128$  pixel field map with  $\Delta = 0.5 \mu\text{m}$  and  $z_0 = 5 \mu\text{m}$ : (a) Calculate the condition number  $\kappa$  of the unregularised Biot–Savart operator. (b) Determine the Wiener parameter  $\lambda$  that limits  $\kappa_{\text{eff}} < 100$ . (c) If CAD data reduces the number of free parameters by  $5\times$ , what is the new effective  $\kappa$ ?

**Hint:**  $\kappa \sim e^{k_{\text{max}} z_0}$  where  $k_{\text{max}} = \pi/\Delta$ . For part (c), use Theorem 15.7.1.

### Problem 15.3: Multi-Physics Depth Discrimination

Two current-carrying wires at depths  $z_1 = 5 \mu\text{m}$  and  $z_2 = 20 \mu\text{m}$  each carry  $I = 1 \text{ mA}$ . The magnetic noise is  $\sigma_B = 50 \text{ nT}$  and thermal noise is  $\sigma_T = 10 \text{ mK}$ . (a) Calculate the expected  $B/T$  ratio for each wire. (b) Determine the SNR of the ratio difference. (c) Can the two wires be distinguished at  $3\sigma$  confidence?

**Hint:** The  $B/T$  ratio scales as  $\sim 1/z$ . Compute  $\sigma_R$  via error propagation of the ratio.

### Problem 15.4: CAD Conditioning Improvement

An IC has metal fill factor  $f = 0.35$  on a  $256 \times 256$  grid with  $z_0 = 8 \mu\text{m}$ . (a) Estimate  $\kappa(\mathbf{G}_{\text{full}})$ . (b) Apply Theorem 15.7.1 to find  $\kappa(\mathbf{G}_{\text{CAD}})$ . (c) Predict  $\Gamma_{\text{inv}}$  using the approximation  $\Gamma_{\text{inv}} \approx 1 - \kappa/\text{SNR}$  for moderate regularisation, given  $\text{SNR} = 100$ .

**Hint:** Use  $\kappa_{\text{CAD}} \leq \kappa_{\text{full}}\sqrt{f}$  and verify the result is physically reasonable ( $0 < \Gamma_{\text{inv}} < 1$ ).

### Problem 15.5: Vector Reconstruction Error Propagation

Each NV axis measurement has independent 5% random error ( $\sigma_{B_i} = 0.05|B_i|$ ). (a) Using Eq. (15.37), derive the error in reconstructed  $B_x$ . (b) Show that the vector reconstruction has uncertainty  $\sigma_{B_x} = (\sqrt{3}/4)\sqrt{\sum_i \sigma_{B_i}^2}$ . (c) For  $|\vec{B}| = 100 \mu\text{T}$ , calculate  $\sigma_{B_x}$  in  $\mu\text{T}$ .

**Hint:** Propagate errors through the linear transformation matrix. Each row of the reconstruction matrix has entries  $\pm\sqrt{3}/4$ .

### Problem 15.6: Depth Disambiguation Requirements

Two current sources at depths  $z_1 = 5 \mu\text{m}$  and  $z_2 = 20 \mu\text{m}$  produce equal  $B_z$  signals at the sensor. Calculate the required  $B/T$  measurement precision to distinguish them at  $3\sigma$  confidence.

**Hint:** The  $B/T$  ratio scales as  $\sim 1/z$ . Require  $|R_1 - R_2| > 3\sigma_R$  where  $\sigma_R$  is the ratio uncertainty.

### Problem 15.7: Measurement Operator Impact on $\Gamma_{\text{inv}}$

A CDR system has  $z_0 = 3 \mu\text{m}$ , NA = 0.5,  $d_{\text{NV}} = 200 \text{ nm}$  (thick CVD layer), pixel size  $\Delta = 0.5 \mu\text{m}$ . (a) Compute  $\tilde{H}_{\text{depth}}(k)$  at  $k = k_c = 1/z_0$  using Eq. (15.15). (b) By what factor does neglecting  $H_{\text{depth}}$  underestimate  $\sigma_J$  at  $k = k_c$ ? (c) If the system claims  $P_{95} = 95\%$  without  $H$  correction, estimate the true coverage.

**Hint:**  $H_{\text{depth}}$  reduces the effective signal at high  $k$ ; ignoring it makes the filter too aggressive, underestimating noise. The coverage drops roughly as  $P_{95,\text{true}} \approx P_{95,\text{claimed}} \times \tilde{H}_{\text{depth}}(k_c)$ .

## References

- [15.1] Tetienne, J.-P. et al., “Quantum imaging of current flow in graphene,” *Science Advances*, vol. 3, no. 4, e1602429, 2017.
- [15.2] Broadway, D.A. et al., “Improved current density and magnetization reconstruction through vector magnetic field measurements,” *Physical Review Applied*, vol. 14, no. 2, 024076, 2020.
- [15.3] Li, Z. et al., “Wide-field current imaging with nitrogen-vacancy centers in diamond,” *Optics Express*, vol. 30, no. 20, pp. 35501–35513, 2022.
- [15.4] Roth, B.J., Sepulveda, N.G., and Wikswo, J.P., “Using a magnetometer to image a two-dimensional current distribution,” *Journal of Applied Physics*, vol. 65, no. 1, pp. 361–372, 1989.
- [15.5] Hansen, P.C., *Discrete Inverse Problems: Insight and Algorithms*, SIAM, 2010.
- [15.6] Boyd, S. et al., “Distributed optimization and statistical learning via the alternating direction method of multipliers,” *Foundations and Trends in Machine Learning*, vol. 3, no. 1, pp. 1–122, 2011.
- [15.7] Maze, J.R. et al., “Nanoscale magnetic sensing with an individual electronic spin in diamond,” *Nature*, vol. 455, no. 7213, pp. 644–647, 2008.
- [15.8] Balasubramanian, G. et al., “Nanoscale imaging magnetometry with diamond spins under ambient conditions,” *Nature*, vol. 455, no. 7213, pp. 648–651, 2008.
- [15.9] Rudin, L.I., Osher, S., and Fatemi, E., “Nonlinear total variation based noise removal algorithms,” *Physica D*, vol. 60, no. 1–4, pp. 259–268, 1992.
- [15.10] Candès, E.J., Romberg, J.K., and Tao, T., “Robust uncertainty principles: exact signal reconstruction from highly incomplete frequency information,” *IEEE Trans. Information Theory*, vol. 52, no. 2, pp. 489–509, 2006.
- [15.11] Glenn, D.R. et al., “Micrometer-scale magnetic imaging of geological samples using a quantum diamond microscope,” *Geochemistry, Geophysics, Geosystems*, vol. 19, no. 4, pp. 1274–1283, 2018.
- [15.12] Ku, M.J.H. et al., “Imaging viscous flow of the Dirac fluid in graphene,” *Nature*, vol. 583, no. 7817, pp. 537–541, 2020.
- [15.13] Nowodzinski, A. et al., “Nitrogen-vacancy centers in diamond for current imaging and analysis of an integrated circuit,” *Microelectronics Reliability*, vol. 55, pp. 1549–1553, 2015.
- [15.14] Midha, D. et al., “Optimized current-density reconstruction for widefield nitrogen-vacancy microscopy,” *Physical Review Applied*, vol. 21, 014036, 2024.
- [15.15] Scholten, S.C. et al., “Widefield quantum microscopy with nitrogen-vacancy centers in diamond: strengths, limitations, and prospects,” *Journal of Applied Physics*, vol. 130, no. 15, 150902, 2021.
- [15.16] Levine, E.V. et al., “QDMlab: a MATLAB toolbox for analyzing quantum diamond microscope data,” available at <https://github.com/QDMlab/QDMlab>, 2022.
- [15.17] Kaipio, J. and Somersalo, E., *Statistical and Computational Inverse Problems*, Springer, 2005.

- [15.18] Tarantola, A., *Inverse Problem Theory and Methods for Model Parameter Estimation*, SIAM, 2005.
- [15.19] Golub, G.H., Heath, M., and Wahba, G., “Generalized cross-validation as a method for choosing a good ridge parameter,” *Technometrics*, vol. 21, no. 2, pp. 215–223, 1979.
- [15.20] Hansen, P.C., “Analysis of discrete ill-posed problems by means of the L-curve,” *SIAM Review*, vol. 34, no. 4, pp. 561–580, 1992.